Development and analysis of the two-regime transient tyre model for combined slip

VEHICLE SYSTEM DYNAMICS
https://doi.org/10.1080/00423114.2022.2057335

Development and analysis of the two-regime transient tyre model for combined slip

Luigi Romano [a], Fredrik Bruzelius[a,b], Mattias Hjort[b] and Bengt Jacobson [a]

[a]Department of Mechanics and Maritime Sciences, Chalmers University of Technology, Gothenburg, Sweden; [b]Driver and Vehicle, VTI Swedish National Road and Transport Research Institute, Gothenburg, Sweden

ABSTRACT

This paper refines the two-regime transient theory developed by Romano et al. [Romano L, Bruzelius F, Jacobson B. Unsteady-state brush theory. Vehicle Syst Dyn. 2020;59:11–29. DOI: 10.1080/00423114.2020.1774625.] to include the effect of combined slip. A nonlinear system is derived that describes the non-steady generation of tyre forces and considers the coupling between the longitudinal and lateral characteristics. The proposed formulation accounts for both the carcass and the bristle dynamics, and represents a generalisation of the single contact point models. A formal analysis is conducted to investigate the effect of the tyre carcass anisotropy on the properties of the system. It is concluded that a fundamental role is played by the ratio between the longitudinal and lateral relaxation lengths. In particular, it is demonstrated that the maximum slip that guarantees (partial) adhesion conditions does not coincide with the stationary value and decreases considerably for highly anisotropic tyres. The dissipative nature of the model is also analysed using elementary tools borrowed from the classic theory for nonlinear systems. A comparison is performed against the single contact point models, showing a good agreement especially towards the full-nonlinear one. Furthermore, compared to the single contact point models, the two-regime appears to be able to better replicate the exact dynamics of the tyre forces predicted by the complete brush theory. Finally, the transient model is partially validated against experimental results.

ARTICLE HISTORY
Received 24 August 2021
Revised 27 December 2021
Accepted 18 March 2022

1. Introduction

Transient tyre behaviour is a crucial aspect in vehicle dynamics, especially in conjunction with severe braking manoeuvres [1]. ABS functions require, indeed, detailed knowledge of tyre states to be effective. Another important aspect to be considered relates to friction estimation, for which several algorithms have been developed. These may, however, mispredict the available friction coefficient if transient phenomena are not accounted for properly in the generation of tyre forces and moments.

The transient dynamics of pneumatic and non-pneumatic tyres [2] is a rather complex phenomenon, which involves several interlinked aspects connected to both the viscoelastic

CONTACT Luigi Romano luigi.romano@chalmers.se

properties of the rubber compound and the non-stationary flow of new material that continuously enters and relinquishes the contact patch [3,4]. An accurate, physically motivated description capable of capturing the salient features of the tyre dynamics often appears to be prohibitive, because of the overwhelming number of parameters that must be taken into account.

In particular, two antipodal approaches may be identified when dealing with transient tyre modelling. The first one consists of a systematic, microscopic analysis of the shear forces developed at the tyre-road interface. Available models explore the phenomenon at a microscopic level and share a great similarity with the ones also used in the context of railway dynamics studies. An example is the classic brush theory [5–9], where the deformation of the tyre tread is modelled by using separate bristles, which alternatively stick to the ground or are in relative motion. The complexity of these formulations – based on the classic theory for partial differential equations – make them unsuitable for simulation purposes and the design of control algorithms.

Different approximated models striving for simplicity have been thus proposed in the literature and are mainly based on the observation that, under certain circumstances, the tyre transient behaviour may be well approximated by those of string or spring-like elements.

The infancy of these models probably dates back to the first studies pioneered by Schlippe [10] and Segel [11], who employed the so-called *stretched-string* tyre model to investigate the non-steady-state response of the tyre to a lateral input [12–19]. Being grounded on a few physical assumptions and relatively easy to interpret, this approach has gained vital importance over the years and is still one of the most effective when it comes to typical situations where the slip parameters are relatively small and the assumption of vanishing sliding holds. Pacejka [20] perfected the analysis by introducing additional bristle elements to extend the stretched-string model towards applications in which the friction limit is exceeded over a finite portion of the contact patch. Typically, enhanced formulations of this time are much more sophisticated and somehow annoying to deal with analytically [21]. However, they led to fundamental results that represent the conceptual basis for simplified models, like the *single contact point* ones [22–24]. In this category also fall some variations that are grounded directly on the simpler brush theory [1,25–29]. In any case, these models are all based on the assumption that the tyre dynamics may be described by a first-order dynamic model, whose main parameter is the so-called *relaxation length*, that is the distance that the tyre needs to travel to develop the 63% of the steady-state forces. In this approach, the transient properties of the tyre force generation are then justified by the presence of an additional deformable element, the tyre carcass, which is held accountable for the whole nonstationary process. In this way, the dual nature of the tyre is mimicked by a series system which behaves as a spring at low rolling speed and as a damper at high speeds. This pragmatic approach leads to a very straightforward model, which generally shows a good agreement with experimental evidence and may be combined with complex analytical expressions for the tyre forces [30]. This legitimates the ubiquitous presence of the single point contact models when it comes to vehicle dynamics simulations. Other formulations, which are based on a similar principle, but introduce higher-order dynamics, are also available in the literature [31,32].

The LuGre friction model [33] has also been proved to be able to replicate the transient behaviour of tyres with high accuracy. The LuGre formulation, in its distributed form, classifies as an enhanced version of the classic brush theory, and accounts for more complex

phenomena, such as the Stribeck effect. Starting from the distributed form, some authors have derived approximated models, based on ordinary differential equations (ODEs), to describe the nonstationary generation of tyre forces [34–42]. This formulation is easier to implement in conventional simulation environments, and is more adequate when it comes to controlling purposes.

Recently, an alternative approach has been proposed by Romano et al. [5] and formalised in the so-called *two-regime theory*. Accordingly, a dynamic model is derived as a functional interpolation between two sets of equations that describe the approximated relationships between the generalised forces and the slip variables at low and high rolling speeds, respectively. The two-regime models consider the transient phenomena connected to the bristle and the tyre carcass dynamics, and represent a generalisation of the single contact point model. However, a major drawback relates to the intrinsic difficulties connected to this approach, which requires inverting the force-slip mappings. This may be often possible only locally, and therefore pose stringent limitations on the general validity of the method. In Romano et al. [5], the derivation of the two-regime tyre models was hence restricted to the case of pure lateral (or longitudinal) slip. In this paper, the authors extend the original formulation to account for the effect of combined translational slips.

The paper is structured as follows: Section 2 recapitulates the salient properties of the brush models and gives a brief overview of the single contact point models. In Section 3, a refined version of the two-regime theory is presented and the notions of *sliding* and *slip functions* are introduced. The nonlinear model for combined slip is then derived in Section 4. The system is analysed with respect to input-to-state stability and the dissipativity. A comparison against the single contact point models is performed in Section 5, showing a good match between the two formulations (Section 5.1). Validation towards experimental results is then carried out in Section 5.2 considering a series of longitudinal manoeuvres. Finally, the main conclusions of the paper are summarised in Section 6.

2. Theory of transient generation of tyre forces

The brush theory represents the mathematical foundation for both the single contact point models and the LuGre-based ones. Therefore, this section introduces the governing partial differential equations (PDEs) of the brush models to the extent that is necessary to understand the paper. A more comprehensive discussion may be found, for example, in [1,6,7,20].

The rolling contact between the tyre and the road takes place inside a small area, called contact patch, and denoted here with $\mathscr{P}$. In the brush theory, it is assumed that $\mathscr{P}$ is a compact, convex subset of $\mathbb{R}^2$, in which the governing PDEs of the model are prescribed. When the camber angle and the turning spin are sufficiently small [6–8], these may be formulated as follows:

$$\boldsymbol{v}_{\mathrm{s}}(\boldsymbol{x},t) = -V_{\mathrm{r}}(t)\left[\boldsymbol{\sigma}(t) + \mathbf{A}_{\varphi}(t)\boldsymbol{x}\right] + \dot{\boldsymbol{\delta}}_{\boldsymbol{t}}(t) + \frac{\partial \boldsymbol{u}_{\boldsymbol{t}}(\boldsymbol{x},t)}{\partial t} - V_{\mathrm{r}}(t)\,\frac{\partial \boldsymbol{u}_{\boldsymbol{t}}(\boldsymbol{x},t)}{\partial x}\,,$$
$$(\boldsymbol{x},t) \in \mathscr{P} \times \mathbb{R}_{>0}. \tag{1}$$

In Equation (1), $\boldsymbol{v}_{\mathrm{s}}(\boldsymbol{x},t) = [\, v_{\mathrm{s}x}(\boldsymbol{x},t) \;\; v_{\mathrm{s}y}(\boldsymbol{x},t) \,]^{\mathrm{T}}$ is the micro-sliding velocity, that is the relative velocity between each point of the contact patch and the road, $\boldsymbol{u}_{\boldsymbol{t}}(\boldsymbol{x},t) = [\, u_x(\boldsymbol{x},t) \;\; u_y(\boldsymbol{x},t) \,]^{\mathrm{T}}$ is

the planar displacement of the bristle inside the contact patch $\mathscr{P}$, $\boldsymbol{\delta}_t(t) = [\,\delta_x(t)\ \delta_y(t)\,]^{\mathrm{T}}$ is the deformation of the tyre carcass (modelled as a linear spring), $V_{\mathrm{r}}(t)$ is the rolling speed, $\boldsymbol{\sigma}(t) = [\,\sigma_x(t)\ \sigma_y(t)\,]^{\mathrm{T}}$ is the slip vector and $\mathbf{A}_\varphi(t)$ is the spin tensor, defined as [7]

$$\mathbf{A}_\varphi(t) = \begin{bmatrix} 0 & -\varphi(t) \\ \varphi(t) & 0 \end{bmatrix}, \tag{2}$$

where $\varphi(t)$ is the spin variable.

The above PDEs come equipped with a boundary (BC) and initial condition (IC):

$$\text{BC}: \quad \boldsymbol{u}_t(\boldsymbol{x}, t) = \mathbf{0}, \quad (\boldsymbol{x}, t) \in \mathscr{L} \times \mathbb{R}_{>0}, \tag{3}$$

$$\text{IC}: \quad \boldsymbol{u}_t(\boldsymbol{x}, 0) = \boldsymbol{u}_{t0}(\boldsymbol{x}), \quad \boldsymbol{x} \in \mathscr{P}. \tag{4}$$

where $\mathscr{L}$ is the leading edge and collects the point of the boundary $\partial\mathscr{P}$ of the contact patch where the bristles enter $\mathscr{P}$.

Equation (1) is valid until the tangential shear stress $\boldsymbol{q}_t(\boldsymbol{x}, t) = \mathbf{K}_t \boldsymbol{u}_t(\boldsymbol{x}, t)$ acting at the coordinate $\boldsymbol{x}$ is smaller or equal than the corresponding friction limit $\mu q_z(\boldsymbol{x}, t)$, where μ is the friction coefficient and $q_z(\boldsymbol{x}, t)$ the vertical pressure acting inside the contact patch. The operator $\mathbf{K}_t \in \mathbb{R}^{2\times 2}$ is a positive definite matrix, usually assumed to be diagonal. As soon as the friction limit is exceeded, indeed, the displacement of the bristle becomes

$$\boldsymbol{u}_t(\boldsymbol{x}, t) = -\mathbf{K}_t^{-1} \mu q_z(\boldsymbol{x}, t) \frac{\boldsymbol{v}_{\mathrm{s}}(\boldsymbol{x}, t)}{v_{\mathrm{s}}(\boldsymbol{x}, t)} \iff v_{\mathrm{s}}(\boldsymbol{x}, t) \neq 0, \tag{5}$$

with $v_{\mathrm{s}}(\boldsymbol{x}, t) \triangleq \left\| \boldsymbol{v}_{\mathrm{s}}(\boldsymbol{x}, t) \right\|_2$.

Owing to the complexity of the problem, a general solution to Equations (1) and (5) in transient conditions is often prohibitive, and might only be attempted numerically. In steady state, when the partial derivative $\partial \boldsymbol{u}_t(\boldsymbol{x}, t)/\partial t$ vanishes or may be neglected, Equations (1) and (5) provide a set of relationships between the tangential forces and moment acting in the contact patch and the slip and spin variables in the form

$$\boldsymbol{F}_t(\boldsymbol{\sigma}, \varphi) = \iint_{\mathscr{P}} \boldsymbol{q}_t(\boldsymbol{x}; \boldsymbol{\sigma}, \varphi)\, \mathrm{d}\boldsymbol{x}, \tag{6a}$$

$$M_z(\boldsymbol{\sigma}, \varphi) = \iint_{\mathscr{P}} (x + \delta_x) q_y\left(\boldsymbol{x}; \boldsymbol{\sigma}, \varphi\right) - (y + \delta_y) q_x\left(\boldsymbol{x}; \boldsymbol{\sigma}, \varphi\right) \mathrm{d}\boldsymbol{x}. \tag{6b}$$

In the single contact point models, the steady-state relationships according to Equations (6a) resulting from the integration over $\mathscr{P}$ play the role of a static nonlinearity that is used to model the tyre forces and moment when subjected to a transient slip.

2.1. The single contact point models

This approach was developed by Higuchi in his excellent dissertation [22] and the subsequent paper [23], and derives directly from the more sophisticated stretched-string and bare-string models, as discussed before. At the time, the effort was towards simplified models characterised by a low computational burden to be employed in vehicle dynamics simulations. The mathematical treatment of the single contact point models presented in this paper mainly refers to the books by Pacejka [8] and Guiggiani [1].

The overall idea behind the single contact point models is to replace the translational slip variable $\boldsymbol{\sigma}$ with the *transient slip vector*

$$\boldsymbol{\sigma}'(t) \triangleq \boldsymbol{\sigma}(t) - \frac{\dot{\boldsymbol{\delta}}_{\boldsymbol{t}}(t)}{V_{\mathrm{r}}(t)}, \tag{7}$$

to account for the additional term due to the carcass deflection. A relationship between the latter and the planar forces is also postulated in the form

$$\boldsymbol{F}_{\boldsymbol{t}}(t) = \mathbf{C}'\boldsymbol{\delta}_{\boldsymbol{t}}(t), \tag{8}$$

where the carcass stiffness matrix $\mathbf{C}'$ is given by

$$\mathbf{C}' = \begin{bmatrix} C'_{xx} & C'_{xy} \\ C'_{yx} & C'_{yy} \end{bmatrix}. \tag{9}$$

The transient slip vector is then used in place of the conventional one in the steady-state expressions for the tangential forces obtained integrating over $\mathscr{P}$ as in Equation (6a), i.e. $\boldsymbol{F}_{\boldsymbol{t}} = \boldsymbol{F}_{\boldsymbol{t}}(\boldsymbol{\sigma}', \varphi)$. Differentiating the planar force vector with respect to the time and combining Equation (7) with (8) yields

$$\dot{\boldsymbol{F}}_{\boldsymbol{t}}\left(\boldsymbol{\sigma}'(t), \varphi(t)\right) = \nabla_{\boldsymbol{\sigma}'}\boldsymbol{F}_{\boldsymbol{t}}\left(\boldsymbol{\sigma}', \varphi\right)^{\mathrm{T}}\dot{\boldsymbol{\sigma}}'(t) + \frac{\partial \boldsymbol{F}_{\boldsymbol{t}}\left(\boldsymbol{\sigma}', \varphi\right)}{\partial \varphi}\dot{\varphi}(t) = V_{\mathrm{r}}(t)\mathbf{C}'\left(\boldsymbol{\sigma}(t) - \boldsymbol{\sigma}'(t)\right). \tag{10}$$

Further simplifications allow to define the concept of the so-called relaxation lengths. In general, the quantities relating to φ are almost irrelevant for the transient generation of tyre forces and may hence be disregarded [1]. Premultiplying by $\mathbf{S}' = \mathbf{C}'^{-1}$ gives

$$\mathbf{S}'\tilde{\mathbf{C}}_{\boldsymbol{\sigma}}\left(\boldsymbol{\sigma}'(t), \varphi(t)\right)\dot{\boldsymbol{\sigma}}'(t) = V_{\mathrm{r}}(t)\left(\boldsymbol{\sigma}(t) - \boldsymbol{\sigma}'(t)\right), \tag{11}$$

where the matrix of the generalised tyre stiffnesses is defined as

$$\tilde{\mathbf{C}}_{\boldsymbol{\sigma}}\left(\boldsymbol{\sigma}', \varphi\right) \triangleq \nabla_{\boldsymbol{\sigma}'}\boldsymbol{F}_{\boldsymbol{t}}\left(\boldsymbol{\sigma}', \varphi\right)^{\mathrm{T}}. \tag{12}$$

The above equation (11) may be recast more conveniently as

$$\tilde{\boldsymbol{\Lambda}}_{\boldsymbol{\sigma}}\left(\boldsymbol{\sigma}'(t), \varphi(t)\right)\dot{\boldsymbol{\sigma}}'(t) + V_{\mathrm{r}}(t)\boldsymbol{\sigma}'(t) = V_{\mathrm{r}}(t)\boldsymbol{\sigma}(t), \tag{13}$$

where the matrix $\tilde{\Lambda}_{\boldsymbol{\sigma}}(\boldsymbol{\sigma}', \varphi)$ of the generalised relaxation lengths is defined as

$$\tilde{\boldsymbol{\Lambda}}_{\boldsymbol{\sigma}}\left(\boldsymbol{\sigma}', \varphi\right) \triangleq \mathbf{S}'\tilde{\mathbf{C}}_{\boldsymbol{\sigma}}\left(\boldsymbol{\sigma}', \varphi\right) = \begin{bmatrix} \tilde{\lambda}_{x\sigma_x}\left(\boldsymbol{\sigma}', \varphi\right) & \tilde{\lambda}_{x\sigma_y}\left(\boldsymbol{\sigma}', \varphi\right) \\ \tilde{\lambda}_{y\sigma_x}\left(\boldsymbol{\sigma}', \varphi\right) & \tilde{\lambda}_{y\sigma_y}\left(\boldsymbol{\sigma}', \varphi\right) \end{bmatrix}. \tag{14}$$

The transient slip calculated by means of Equation (13) is used as input to a steady-state model for the tyre forces. This variant of the single contact point model is referred to as *full-nonlinear*, since the matrix $\tilde{\Lambda}_{\boldsymbol{\sigma}}(\boldsymbol{\sigma}', \varphi)$ is itself a function of $\boldsymbol{\sigma}'$. In practical applications, the matrix of the generalised stiffnesses is approximated with the conventional one $\mathbf{C}_{\boldsymbol{\sigma}} =$

$\tilde{\mathbf{C}}_{\boldsymbol{\sigma}}(\mathbf{0}, 0)$, and hence the matrix $\tilde{\Lambda}_{\boldsymbol{\sigma}}$ becomes constant, that is $\tilde{\Lambda}_{\boldsymbol{\sigma}}(\boldsymbol{\sigma}', \varphi) \equiv \Lambda_{\boldsymbol{\sigma}}$, with $\Lambda_{\boldsymbol{\sigma}}$ reading

$$\boldsymbol{\Lambda}_{\boldsymbol{\sigma}} = \mathbf{S}'\mathbf{C}_{\boldsymbol{\sigma}} = \begin{bmatrix} \lambda_{x\sigma_x} & \lambda_{x\sigma_y} \\ \lambda_{y\sigma_x} & \lambda_{y\sigma_y} \end{bmatrix} = \begin{bmatrix} S'_{xx}C_{x\sigma_x} + S'_{xy}C_{y\sigma_x} & S'_{xx}C_{x\sigma_y} + S'_{xy}C_{y\sigma_y} \\ S'_{yx}C_{x\sigma_x} + S'_{yy}C_{y\sigma_x} & S'_{yx}C_{x\sigma_y} + S'_{yy}C_{y\sigma_y} \end{bmatrix}. \tag{15}$$

This model variation is often referred to as *semi-nonlinear single contact point*. Additionally, if the stiffness matrix of the tyre carcass is diagonal, that is

$$\mathbf{C}' = \begin{bmatrix} C'_x & 0 \\ 0 & C'_y \end{bmatrix}, \tag{16}$$

the matrix $\Lambda_{\boldsymbol{\sigma}}$ further reduces to

$$\boldsymbol{\Lambda}_{\boldsymbol{\sigma}} = \begin{bmatrix} \lambda_{x\sigma_x} & \lambda_{x\sigma_y} \\ \lambda_{y\sigma_x} & \lambda_{y\sigma_y} \end{bmatrix} = \begin{bmatrix} \dfrac{C_{x\sigma_x}}{C'_x} & \dfrac{C_{x\sigma_y}}{C'_x} \\ \dfrac{C_{y\sigma_x}}{C'_y} & \dfrac{C_{y\sigma_y}}{C'_y} \end{bmatrix}. \tag{17}$$

Up to this point, it should be acknowledged that the single contact point models well approximate the real dynamics of a tyre in transient slip conditions. However, from a pure conceptual viewpoint, this approach is wrong. Indeed, the transient of the bristles is always neglected in this case, despite being an essential part of the transient process of forces and moments generation. Furthermore, the single point contact models do not explain the empirical and theoretical presence of transient phenomena in e.g. railway applications, where the wheel may be approximated as a rigid body to some extent.

It is quite simple, in fact, to show that disregarding the transient connected to the deflection of the bristles automatically implies steady-state conditions for the tangential forces exerted at the tyre-road interface. Indeed, under reasonable assumptions, the time derivatives of the planar force vector $\boldsymbol{F}_{\boldsymbol{t}}(t)$ and the self-aligning moment $M_z(t)$ in Equations (6a) read, respectively:

$$\dot{\boldsymbol{F}}_{\boldsymbol{t}}(t) = \iint_{\mathscr{P}} \frac{\partial \boldsymbol{q}_{\boldsymbol{t}}(\boldsymbol{x}, t)}{\partial t}\, \mathrm{d}\boldsymbol{x}, \tag{18a}$$

$$\dot{M}_z(t) = \iint_{\mathscr{P}} x\, \frac{\partial q_y(\boldsymbol{x}, t)}{\partial t} - y\, \frac{\partial q_x(\boldsymbol{x}, t)}{\partial t}\, \mathrm{d}\boldsymbol{x}. \tag{18b}$$

Clearly, since $\boldsymbol{F}_{\boldsymbol{t}}(t) = \mathbf{C}'\boldsymbol{\delta}_{\boldsymbol{t}}(t)$, from Equation (18a), it is immediate to infer that

$$\dot{\boldsymbol{\delta}}_{\boldsymbol{t}}(t) = \mathbf{S}'\dot{\boldsymbol{F}}_{\boldsymbol{t}}(t) = \mathbf{0}, \tag{19}$$

and therefore also $\dot{M}_z(t) = 0$. The above results demonstrate the fundamental role played by the transient deflection of the bristle in the nonsteady-state generation of tyre forces. It seems thus reasonable to account for this effect even when approaching a simplified model to describe nonstationary processes related to tyre dynamics. The spontaneous question is how to derive a consistent set of equations to model the phenomenon properly. The solution proposed by the authors is presented in the next Section 3 and represents a further generalisation of that already sketched in Romano et al. [5].

3. Refined two-regime theory

The main scope of this paper consists of the derivation and the analysis of the two-regime model for the case of combined translational slips. The investigation is conducted from the perspective of nonlinear systems. To this end, the general idea behind the theory introduced by Romano et al. [5] is succinctly recapitulated. In this paper, however, an alternative and more comprehensive approach to derive the governing equations of the two-regime model is proposed.

To start, the existence of two implicit representations is assumed of the form:

$$\check{\boldsymbol{\Upsilon}}\left(V_{\mathrm{r}}\boldsymbol{\sigma}, V_{\mathrm{r}}\varphi, \dot{\boldsymbol{F}}_{\boldsymbol{t}}, \dot{M}_z\right) = \mathbf{0}, \tag{20a}$$

$$\hat{\boldsymbol{\Upsilon}}(\boldsymbol{\sigma}, \varphi, \boldsymbol{F}_{\boldsymbol{t}}, M_z) = \mathbf{0}. \tag{20b}$$

The above equations (20) postulate certain relationships between the slip variables and tyre characteristics acting at the tyre contact patch. Ideally, they should approximate the tyre dynamics at low and high values of the rolling speed.

From Equations (20), it is possible to locally express the variables $(\boldsymbol{\sigma}, \varphi)$ invoking the Implicit Function Theorem. In particular, Equation (20a) gives

$$\boldsymbol{\sigma} = \frac{1}{V_{\mathrm{r}}}\check{\boldsymbol{\sigma}}\left(\dot{\boldsymbol{F}}_{\boldsymbol{t}}, \dot{M}_z\right), \tag{21a}$$

$$\varphi = \frac{1}{V_{\mathrm{r}}}\check{\varphi}\left(\dot{\boldsymbol{F}}_{\boldsymbol{t}}, \dot{M}_z\right), \tag{21b}$$

where the functions $\check{\boldsymbol{\sigma}}(\cdot,\cdot) = [\,\check{\sigma}_x(\cdot,\cdot)\ \check{\sigma}_y(\cdot,\cdot)\,]^{\mathrm{T}}$ and $\check{\varphi}(\cdot,\cdot)$ are called *sliding functions*. On the other hand, Equation (20b) yields

$$\boldsymbol{\sigma} = \hat{\boldsymbol{\sigma}}(\boldsymbol{F}_{\boldsymbol{t}}, M_z), \tag{22a}$$

$$\varphi = \hat{\varphi}(\boldsymbol{F}_{\boldsymbol{t}}, M_z), \tag{22b}$$

in which $\hat{\boldsymbol{\sigma}}(\cdot,\cdot) = [\,\hat{\sigma}_x(\cdot,\cdot)\ \hat{\sigma}_y(\cdot,\cdot)\,]^{\mathrm{T}}$ and $\hat{\varphi}(\cdot,\cdot)$ are referred to as *slip functions*. It is worth pointing out that Equations (21) and (22) are valid in turn for low and high values of V_{r}.

Interpolating between Equations (21) and (22) yields the two-regime tyre models:

$$\boldsymbol{\sigma} = \frac{1}{V_{\mathrm{r}}}\check{\boldsymbol{\sigma}}\left(\dot{\boldsymbol{F}}_{\boldsymbol{t}}, \dot{M}_z\right) + \hat{\boldsymbol{\sigma}}(\boldsymbol{F}_{\boldsymbol{t}}, M_z), \tag{23a}$$

$$\varphi = \frac{1}{V_{\mathrm{r}}}\check{\varphi}\left(\dot{\boldsymbol{F}}_{\boldsymbol{t}}, \dot{M}_z\right) + \hat{\varphi}(\boldsymbol{F}_{\boldsymbol{t}}, M_z), \tag{23b}$$

Equations (23) allow to express the slips $(\boldsymbol{\sigma}, \varphi)$ as a weighted combination of two different vector-valued functions: the first captures the tyre behaviour at low rolling speed, the second one, instead, gives an approximation at high rolling speeds. They also provide a set of ODEs for the tyre characteristics. If the sliding functions have an isolated equilibrium at the origin, it is clear that the equilibria of the ODEs (23) coincide with the steady-state relationships for the tyre forces and moment.

The main limitation of this approach consists in the fact an explicit representation of $\check{\boldsymbol{\Upsilon}}(\cdot,\cdot,\cdot,\cdot)$ and $\hat{\boldsymbol{\Upsilon}}(\cdot,\cdot,\cdot,\cdot)$ might often be obtained only locally.

In the subsequent subsections 3.1 and 3.2, respectively, the sliding and slip functions will be derived.

3.1. The sliding functions

At low, speed, the sliding functions may be sought as follows:

$$\begin{bmatrix} \check{\boldsymbol{\sigma}}\left(\dot{\boldsymbol{F}}_{\boldsymbol{t}}, \dot{M}_z\right) \\ \check{\varphi}\left(\dot{\boldsymbol{F}}_{\boldsymbol{t}}, \dot{M}_z\right) \end{bmatrix} = \begin{bmatrix} \mathbf{S}'_{\boldsymbol{F}} & \mathbf{S}'_{M} \\ \mathbf{S}'_{\varphi \boldsymbol{F}} & S'_{\varphi M} \end{bmatrix} \begin{bmatrix} \dot{\boldsymbol{F}}_{\boldsymbol{t}} \\ \dot{M}_z \end{bmatrix}, \tag{24}$$

where the matrix on the right-hand side is nonsingular, and $\mathbf{S}'_{\boldsymbol{F}}$, $\mathbf{S}'_{M}$, $\mathbf{S}'_{\varphi \boldsymbol{F}}$ and $S'_{\varphi M}$ represent generalised compliances. The derivation of Equation (24) is detailed in Appendix 1. The system described by Equation (24) is linear, and, as already anticipated, obviously admits a unique equilibrium in the origin.

Furthermore, when the spin slip φ and the self-aligning moment M_z are neglected, Equation (24) reduces to a relationship between the translational sliding functions and the tangential forces in the form

$$\check{\boldsymbol{\sigma}}\left(\dot{\boldsymbol{F}}_{\boldsymbol{t}}\right) = \mathbf{S}'_{\boldsymbol{F}} \dot{\boldsymbol{F}}_{\boldsymbol{t}} = \left(\frac{1}{A_{\mathscr{P}}} \mathbf{K}_{\boldsymbol{t}}^{-1} + \mathbf{S}'\right) \dot{\boldsymbol{F}}_{\boldsymbol{t}}, \tag{25}$$

where $A_{\mathscr{P}}$ is the area of the contact patch $\mathscr{P}$.

Example 3.1: For an tyre with isotropic tread, rectangular contact patch and diagonal stiffness matrix for the tyre carcass $\mathbf{C}'$, the matrix $\mathbf{S}'_{\boldsymbol{F}}$ reads specifically

$$\mathbf{S}'_{\boldsymbol{F}} = \begin{bmatrix} \dfrac{aC'_x + C_\sigma}{C'_x C_\sigma} & 0 \\ 0 & \dfrac{aC'_y + C_\sigma}{C'_y C_\sigma} \end{bmatrix}, \tag{26}$$

where $C_\sigma = 4a^2 bk$, a and b are the contact patch semilength and semiwidth, respectively, and k is the bristle stiffness.

For convenience, the following Assumption 3.1 is retained in the remaining of the paper.

Assumption 3.1: The matrices $\mathbf{K}_{\boldsymbol{t}} \in \mathbb{R}^{2\times 2}$ and $\mathbf{C}' \in \mathbb{R}^{2\times 2}$ are symmetric and positive definite.

From Equation (25), it may be inferred that the above Assumption 3.1 ensures that $\mathbf{S}'_{\boldsymbol{F}}$ is also positive definite.

3.2. The slip functions

In steady-state conditions, the explicit relationships between the tangential forces and the self-aligning moment and the slip variables are often known in the form

$$\boldsymbol{F}_{\boldsymbol{t}} = \hat{\boldsymbol{F}}_{\boldsymbol{t}}(\boldsymbol{\sigma}, \varphi), \tag{27a}$$

$$M_z = \hat{M}_z(\boldsymbol{\sigma}, \varphi), \tag{27b}$$

where $\hat{\boldsymbol{F}}_{\boldsymbol{t}}(\boldsymbol{\sigma},\varphi)$, $\hat{M}_z(\boldsymbol{\sigma},\varphi)$ are obtained by integration over $\mathscr{P}$ as in Equation (6) or using empirical formulae[1]. Inverting Equations (27) yields a local representation of the translational slip $\boldsymbol{\sigma}$ and spin φ in the form of slip functions $(\hat{\boldsymbol{\sigma}},\hat{\varphi})$.

This paper restricts to the case of pure translational slip, that is disregards the (usually small) contribution due to spin. Furthermore, it considers steady-state relationships as in Assumption 3.2.

Assumption 3.2: In steady-state conditions, the tyre forces may be described by a relationship of the type

$$\boldsymbol{F}_{\boldsymbol{t}} = \hat{\boldsymbol{F}}_{\boldsymbol{t}}(\boldsymbol{\sigma}) = \hat{F}_{\boldsymbol{t}}(\sigma)\frac{\boldsymbol{\sigma}}{\sigma}, \tag{28}$$

where $\hat{F}_{\boldsymbol{t}}(\sigma) \triangleq \left\|\hat{\boldsymbol{F}}_{\boldsymbol{t}}(\boldsymbol{\sigma})\right\|_2$ and $\sigma \triangleq \|\boldsymbol{\sigma}\|_2$. Furthermore, it is assumed that $\hat{F}_{\boldsymbol{t}} \in \mathcal{K}$ when σ is restricted to the interval $[0, \sigma^{\text{peak}})$, for some value $\sigma^{\text{peak}} > 0$.

Tyre functions of the same type as in Equation (28) usually describe the forces when the tread is assumed to be isotropic. According to Assumption 3.2, Equation (28) is also invertible in the range $\sigma \in [0, \sigma^{\text{peak}})$, where σ^{peak} corresponds to the value for which $F_{\boldsymbol{t}} \triangleq \|\boldsymbol{v}_{\boldsymbol{t}}\|_2$ attains its maximum value, that is $\hat{F}_{\boldsymbol{t}}(\sigma^{\text{peak}}) = F_{\boldsymbol{t}}^{\max} \triangleq \mu_{\text{peak}} F_z$. The values σ^{peak} is generally smaller than the critical slip value σ^{cr} that causes total sliding inside the contact patch, as shown in Figure 1.

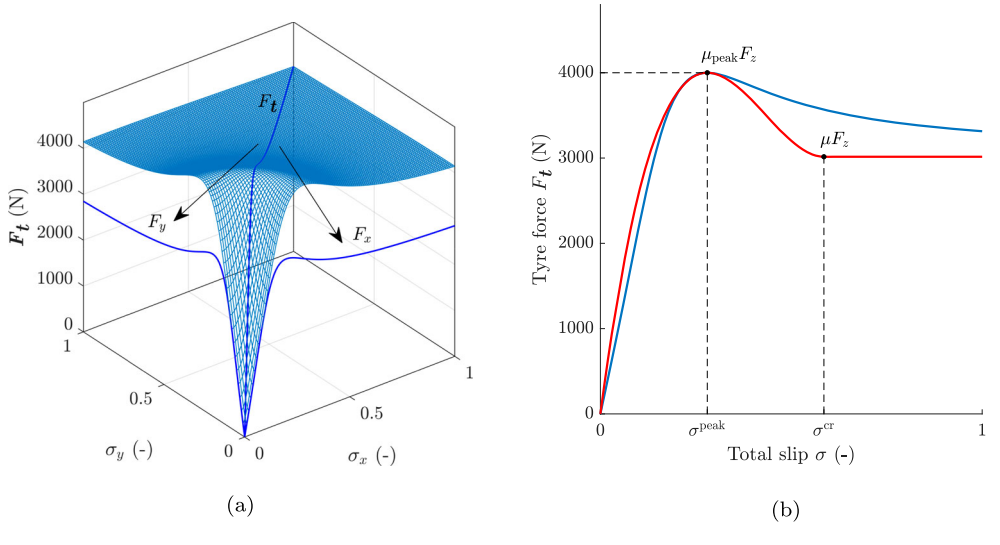

Figure 1. A qualitative example of steady-state models for the tangential tyre forces satisfying Assumption 3.2. Figure 1(a) illustrates a tyre surface $F_{\boldsymbol{t}} = \hat{F}_{\boldsymbol{t}}(\sigma)$ according to Equation (28), with its components projected in longitudinal and lateral directions. Figure 1(b) exemplifies two different tyre models: a simplified version of Pacejka's Magic Formula (blue line) and a brush model with different static and dynamic friction coefficients (red line). The models share the same peak value $\mu_{\text{peak}} F_z$ for $\sigma = \sigma^{\text{peak}}$; however, whilst the brush models predict total sliding in the contact patch for $\sigma > \sigma^{\text{cr}}$, Pacejka's Magic Formula does not. (a) Tyre force surface $F_{\boldsymbol{t}} = \hat{F}_{\boldsymbol{t}}(\sigma)$ according to Equation (28) with projections F_x and F_y for $\sigma_x = \sigma_y$. (b) Two steady-state tyre models satisfying Assumption 3.2.

The inverse relationship of Equation (28) may be found as

$$\boldsymbol{\sigma} = \hat{\boldsymbol{\sigma}}(\boldsymbol{F_t}) = \hat{\sigma}(F_t)\frac{\boldsymbol{F_t}}{F_t}, \quad F_t \in \left[0, \mu_{\text{peak}} F_z\right), \tag{29}$$

being $\hat{\sigma}(\cdot) \triangleq \hat{F}_t^{-1}(\cdot)$ also a $\mathcal{K}$-class function. Often, the expression for the function $\hat{\sigma}(\cdot)$ cannot be derived in closed-form. Analytical approximations may be, however, constructed using fixed-point theorems [43]. There are, of course, exceptional cases in which $\hat{\sigma}(\cdot)$ may be easily determined.

Example 3.2: According to the brush models, for an isotropic tyre with a rectangular contact patch and unique friction coefficient, the tangential forces depend upon the translational slip as follows:

$$\boldsymbol{F_t} = \hat{\boldsymbol{F}}_t(\boldsymbol{\sigma}) = \hat{F}_t(\sigma)\frac{\boldsymbol{\sigma}}{\sigma} = C_\sigma \boldsymbol{\sigma}\left[1 - \frac{\sigma}{\sigma^{\text{cr}}} + \frac{1}{3}\left(\frac{\sigma}{\sigma^{\text{cr}}}\right)^2\right], \quad \sigma \in [0, \sigma^{\text{cr}}), \tag{30}$$

where $\sigma^{\text{cr}} \triangleq 3\mu F_z / C_\sigma$. It should be noticed that, for the model in Equation (30), $\sigma^{\text{peak}} \equiv \sigma^{\text{cr}}$. Accordingly for larger values of the slip, i.e. $\sigma \geq \sigma^{\text{cr}}$, the tangential force equals the peak value $\mu_{\text{peak}} F_z \equiv \mu F_z$, and is oriented as the slip vector, that is $\boldsymbol{F_t} = \mu F_z \boldsymbol{\sigma}/\sigma$. The inverse relationship of Equation (30) reads [44]

$$\boldsymbol{\sigma} = \hat{\boldsymbol{\sigma}}(\boldsymbol{F_t}) = \hat{\sigma}(F_t)\frac{\boldsymbol{F_t}}{F_t} = \sigma^{\text{cr}}\left(1 - \sqrt[3]{1 - \frac{F_t}{\mu F_z}}\right)\frac{\boldsymbol{F_t}}{F_t}, \quad F_t \in [0, \mu F_z), \tag{31}$$

where $\mu_{\text{peak}} \equiv \mu$ (the peak friction coefficient equals the actual one). Clearly, the function $\hat{\boldsymbol{\sigma}}(\cdot)$ in the above equation (31) is of the type of that in Equation (29).

Figure 2 illustrates the sigma functions $\hat{\boldsymbol{\sigma}}(\cdot)$ and the function $\hat{\sigma}(\cdot)$ in Example 3.2 for the case of pure translational slip.

4. Two-regime tyre model for combined slip

Taking advantage of the theoretical framework developed in Section 3, this paper now moves to derive and analyse the nonlinear system describing the transient tyre dynamics at combined slip. Plugging Equations (26) and (31) into (23a) yields the two-regime tyre model for combined slip:

$$\dot{\boldsymbol{F}}_t(t) = V_{\text{r}}(t)\mathbf{C}'_{\boldsymbol{\sigma}}\left[\boldsymbol{\sigma}(t) - \hat{\boldsymbol{\sigma}}\left(\boldsymbol{F_t}(t)\right)\right], \tag{32}$$

where the matrix $\mathbf{C}'_{\boldsymbol{\sigma}}$ is defined as

$$\mathbf{C}'_{\boldsymbol{\sigma}} = \begin{bmatrix} C'_{x\sigma_x} & C'_{x\sigma_y} \\ C'_{y\sigma_x} & C'_{y\sigma_y} \end{bmatrix} = \begin{bmatrix} C'_{\sigma_x} & 0 \\ 0 & C'_{\sigma_y} \end{bmatrix} \triangleq \mathbf{S}'^{-1}_{\boldsymbol{F}}. \tag{33}$$

The above equation may be reinterpreted in terms of enhanced relaxation lengths premultiplying both sides by $\Lambda'_{\boldsymbol{\sigma}} \triangleq \mathbf{C}_{\boldsymbol{\sigma}}\mathbf{S}'_{\boldsymbol{F}}$. This yields

$$\boldsymbol{\Lambda}'_{\boldsymbol{\sigma}}\dot{\boldsymbol{F}}_t(t) = V_{\text{r}}(t)C_\sigma\left[\boldsymbol{\sigma}(t) - \hat{\boldsymbol{\sigma}}\left(\boldsymbol{F_t}(t)\right)\right], \tag{34}$$

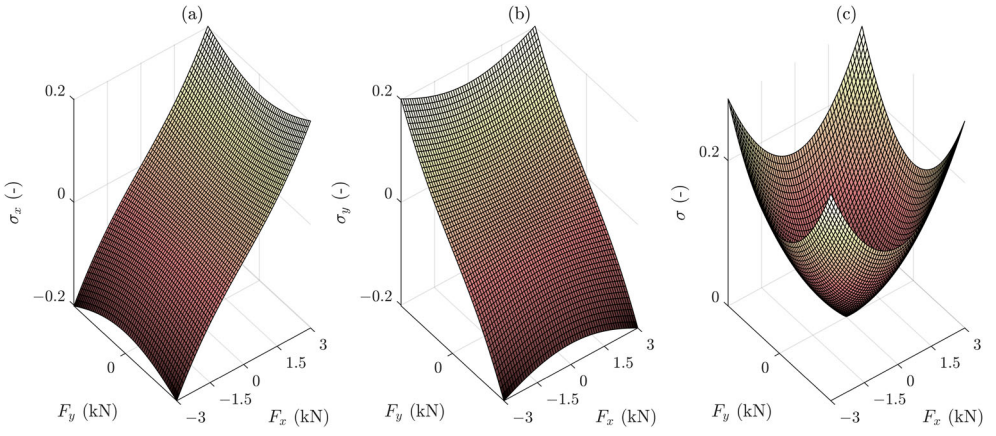

Figure 2. Slip variables expressed as sigma functions $\sigma_x = \hat{\sigma}_x(\boldsymbol{F_t})$, $\sigma_y = \hat{\sigma}_y(\boldsymbol{F_t})$ and $\sigma = \hat{\sigma}(\boldsymbol{F_t})$ (Figures 2(a,b) and (c), respectively) as functions of the longitudinal and lateral tyre force given as in Equations (31). Tyre parameters: $C_\sigma = 30,000$ N, $\mu = 1$, $\sigma^{\mathrm{cr}} = 0.3$, $F_z = 3000$ N.

where the matrix

$$\boldsymbol{\Lambda}'_{\boldsymbol{\sigma}} = \begin{bmatrix} \lambda'_{x\sigma_x} & \lambda'_{x\sigma_y} \\ \lambda'_{y\sigma_x} & \lambda'_{y\sigma_y} \end{bmatrix} \tag{35}$$

collects the enhanced relaxation terms. These relaxation lengths are referred to as enhanced because they also account for the transient of the bristles in the contact patch [5]. A fundamental role in the transient generation of the tyre forces is played by the relaxation ratio χ_λ, defined as

$$\chi_\lambda = \frac{\lambda_{\min}\left(\mathbf{C}'_{\boldsymbol{\sigma}}\right)}{\lambda_{\max}\left(\mathbf{C}'_{\boldsymbol{\sigma}}\right)}, \tag{36}$$

where $\lambda_{\max}(\cdot)$ and $\lambda_{\min}(\cdot)$ denote the maximum and minimum eigenvalues of a matrix, respectively. By Assumption $\mathbf{C}'_{\boldsymbol{\sigma}}$ is symmetric and positive definite, and therefore $\lambda_{\max}(\mathbf{C}'_{\boldsymbol{\sigma}})$ and $\lambda_{\min}(\mathbf{C}'_{\boldsymbol{\sigma}})$ in Equation (36) are always positive real.

Example 4.1: Combining the results from Examples 3.1 and 3.2, the matrices $\mathbf{C}'_{\boldsymbol{\sigma}}$ becomes

$$\mathbf{C}'_{\boldsymbol{\sigma}} = \begin{bmatrix} C'_{\sigma_x} & 0 \\ 0 & C'_{\sigma_y} \end{bmatrix} = \begin{bmatrix} \dfrac{C'_x C_\sigma}{aC'_x + C_\sigma} & 0 \\ 0 & \dfrac{C'_y C_\sigma}{aC'_y + C_\sigma} \end{bmatrix}, \tag{37}$$

where it has been renamed $C'_{\sigma_x} \triangleq C'_{x\sigma_x}$ and $C'_{\sigma_y} \triangleq C'_{y\sigma_y}$ without ambiguity. Accordingly, the matrix of enhanced relaxation lengths reads

$$\boldsymbol{\Lambda}'_{\boldsymbol{\sigma}} = \begin{bmatrix} \lambda'_{\sigma_x} & 0 \\ 0 & \lambda'_{\sigma_y} \end{bmatrix} = \begin{bmatrix} \dfrac{C_\sigma}{C'_{\sigma_x}} & 0 \\ 0 & \dfrac{C_\sigma}{C'_{\sigma_y}} \end{bmatrix}, \tag{38}$$

where again it has been renamed $\lambda'_{\sigma_x} \triangleq \lambda'_{x\sigma_x}$ and $\lambda'_{\sigma_y} \triangleq \lambda'_{y\sigma_y}$, and the slip function $\hat{\boldsymbol{\sigma}}(\cdot)$ reading as in Equation (31). In this case, the relaxation ratio may also be interpreted as

$$\chi_\lambda \equiv \frac{C'_{\min}}{C'_{\max}} \equiv \frac{\lambda'_{\min}}{\lambda'_{\max}}, \tag{39}$$

where $C'_{\max} \triangleq \max\{C'_{\sigma_x}, C'_{\sigma_y}\}$ and $C'_{\min} \triangleq \min\{C'_{\sigma_x}, C'_{\sigma_y}\}$. Similarly, $\lambda'_{\max} \triangleq \max\{\lambda'_{\sigma_x}, \lambda'_{\sigma_y}\}$ and $\lambda'_{\min} \triangleq \min\{\lambda'_{\sigma_x}, \lambda'_{\sigma_y}\}$. Therefore, the relaxation ratio χ_λ condenses the two different relaxation behaviours of the tyre in longitudinal and lateral direction. Usually, $C'_x > C'_y$, which also implies $\lambda_{\sigma_y} > \lambda_{\sigma_x}$.

4.1. Model analysis

Now the authors proceed to the formal analysis of the two-regime model. There are two aspects to investigate. The first one relates to the trajectories of the system described by Equation (32) in presence of finite slip, which will be treated as a given input. Ideally, the model should be able to replicate the transient behaviour of the tyre during nominal operational conditions. For the steady-state model, this translates into the requirement $F_{\boldsymbol{t}} < \mu_{\text{peak}} F_z$, which is equivalent to $\sigma < \sigma^{\text{peak}}$. In transient conditions, it is not obvious that the fulfillment of $\sup_s \sigma(s) < \sigma^{\text{peak}}$ also implies $F_{\boldsymbol{t}}(s) < \mu_{\text{peak}} F_z$. Therefore, an equivalent *transient critical* value for the slip should be estimated.

The second aspect concerns the dissipative nature of the model. Finite slip causes losses at the tyre contact patch, known as slip losses. Intuitively, the power generated by the slip should not be expected to be entirely converted into useful tangential forces.

A major issue with the system described by Equation (32), however, connects to the presence of the term $F_{\boldsymbol{t}}$ appearing in the denominator. This is responsible for some difficulties encountered in simulation, since the situation $F_{\boldsymbol{t}} = 0$ is not handled properly. To overcome this issue, the original sigma functions $\hat{\boldsymbol{\sigma}}(\cdot)$ in Equation (32) may be conveniently replaced with

$$\hat{\boldsymbol{\sigma}}_\epsilon(\boldsymbol{F}_{\boldsymbol{t}}; \epsilon) \triangleq \hat{\sigma}(F_{\boldsymbol{t}}) \frac{\boldsymbol{F}_{\boldsymbol{t}}}{F_{\boldsymbol{t}} + \epsilon}, \tag{40}$$

where $\epsilon \in \mathbb{R}_{>0}$ is an arbitrary small constant. In the above equation (40), the constant ϵ in $\hat{\boldsymbol{\sigma}}_\epsilon(\cdot; \epsilon)$ should be regarded as a parameter. Owing to Equation (40), a modified model may be considered as

$$\dot{\boldsymbol{F}}_{\boldsymbol{t}}(t) = V_{\text{r}}(t) \mathbf{C}'_{\boldsymbol{\sigma}} \left[\boldsymbol{\sigma}(t) - \hat{\boldsymbol{\sigma}}_\epsilon \left(\boldsymbol{F}_{\boldsymbol{t}}(t); \epsilon \right) \right]. \tag{41}$$

For what follows, it may also be useful to introduce the function $\hat{\sigma}_\epsilon(\cdot; \epsilon)$ defined as

$$\hat{\sigma}_\epsilon(F_{\boldsymbol{t}}; \epsilon) \triangleq \hat{\sigma}(F_{\boldsymbol{t}}) \frac{F_{\boldsymbol{t}}}{F_{\boldsymbol{t}} + \epsilon}. \tag{42}$$

It should be observed that Assumption 3.2 implies that $\hat{\sigma}_\epsilon(\cdot; \epsilon)$ in Equation (42) is also a $\mathcal{K}$-class function. The subsequent analysis will be therefore conducted concerning the modified model described by Equation (41) rather than the original one. The latter represents a particular case of the former for $\epsilon \to 0^+$.

4.1.1. Friction limit

In analogy to the steady-state model, an upper bound for the slip input that guarantees that the total tangential force never reaches the friction limit, that is $F_{\boldsymbol{t}} < \mu_{\text{peak}} F_z$, should be estimated. To proceed, the notion of friction circle is formalised as the set

$$\mathcal{C}_\mu \triangleq \left\{ \boldsymbol{F}_{\boldsymbol{t}} \in \mathbb{R}^2 \;\middle|\; F_{\boldsymbol{t}} \leq \mu_{\text{peak}} F_z \right\}, \tag{43}$$

whose interior is denoted by $\overset{\circ}{\mathcal{C}}_\mu$. The idea is now to understand when $\overset{\circ}{\mathcal{C}}_\mu$ is an invariant set for $\boldsymbol{F}_{\boldsymbol{t}}(t)$, that is which pairs of initial conditions $\boldsymbol{F}_{\boldsymbol{t}0} = \boldsymbol{F}_{\boldsymbol{t}}(t_0) \in \overset{\circ}{\mathcal{C}}_\mu$ and inputs $\boldsymbol{\sigma}(t)$ ensure $\boldsymbol{F}_{\boldsymbol{t}}(t)$ to stay indefinitely in $\overset{\circ}{\mathcal{C}}_\mu$ for all $t \geq t_0$. Sufficient conditions are stated in the following Theorem 4.1.

Theorem 4.1: *Assume that $\sigma(t)$ satisfies*

$$\sup_{t \geq t_0} \sigma(t) < \sigma_\chi \triangleq \psi \chi_\lambda \sigma^{\text{cr}} \frac{1}{1 + \epsilon / \left(\mu_{\text{peak}} F_z \right)}, \tag{44}$$

where $\psi \in (0,1)$ is arbitrary small. If $\boldsymbol{F}_{\boldsymbol{t}0} \in \overset{\circ}{\mathcal{C}}_\mu$, then $\boldsymbol{F}_{\boldsymbol{t}}(t) \in \overset{\circ}{\mathcal{C}}_\mu$ for all $t \geq t_0$. Furthermore, the system described by Equation (41) is input-to-state stable[2] with $\gamma : [0, \sigma_\chi) \times \mathbb{R}_{>0} \mapsto [0, \mu_{\text{peak}} F_z)$ given by

$$\gamma(\sigma; \epsilon) \triangleq \begin{cases} 0, & \sigma = 0, \\ \sigma_\epsilon^{-1} \left(\dfrac{\sigma}{\psi \chi_\lambda}; \epsilon \right), & \sigma \in \left(0, \sigma_\chi \right), \end{cases} \tag{45}$$

and satisfying

$$\lim_{\epsilon \to 0^+} \gamma(\sigma; \epsilon) = \hat{F}_{\boldsymbol{t}} \left(\frac{\sigma}{\psi \chi_\lambda} \right). \tag{46}$$

Proof: The proof is given in Appendix 2. ■

The above Theorem 4.1 provides an upper bound σ_χ on the slip input. As it may be observed from Equation (44), σ_χ depends on three parameters: ψ, ϵ and χ_λ. The first two do not deserve particular attention, since they may be chosen arbitrarily. On the other hand, the relaxation ratio χ_λ is a structural parameter and accounts for the anisotropy of the tyre carcass. Specifically, according to Equation (44), lower values of χ_λ correspond to smaller admissible inputs σ_χ, above which full sliding may occur inside the contact patch.

Figure 3 provides a graphical interpretation of this result for different relaxation ratios χ_λ for a tyre with isotropic tread and rectangular patch (model of Example 4.1, with $\mu_{\text{peak}} \equiv \mu$ and $\hat{\boldsymbol{\sigma}}(\cdot)$ replaced by $\hat{\boldsymbol{\sigma}}_\epsilon(\cdot; \epsilon)$) with critical slip $\sigma^{\text{peak}} \equiv \sigma^{\text{cr}} = 0.3$. In the left-hand side plots, the circles depicted in red represent the friction circle $\mathcal{C}_\mu$, whilst the green area the sets of attainable steady-state forces for $\sigma < \sigma_\chi$, that is $\boldsymbol{F}_{\boldsymbol{t}}(t) \in \overset{\circ}{\mathcal{C}}_\chi$, with $\mathcal{C}_\chi \triangleq \{ \boldsymbol{F}_{\boldsymbol{t}} \in \mathbb{R}^2 \mid F_{\boldsymbol{t}} \leq \sigma_\epsilon^{-1}(\sigma_\chi; \epsilon) \}$. The set $\mathcal{C}_\chi$ is defined here as the *relaxation circle*. On the right-hand side of Figure 3, the corresponding maximum values $F_{\boldsymbol{t}}(\sigma_\chi)$ are shown,

which amount to the 70.4, 92.1 and 98.44% of the peak force. It is worth noticing that, for a tyre with isotropic carcass, in general $\sigma_\chi \equiv \sigma^{\text{peak}}$ when $\epsilon = 0$ and $\psi \to 1$. The same condition holds for the one-dimensional models already presented in [5], for which the parameter ϵ is not needed.

When the slip input exceeds σ_χ, it is not obvious that $F_{\boldsymbol{t}}(t) < \mu_{\text{peak}} F_z$. Again for the isotropic model in Example 4.1 with $\mu_{\text{peak}} \equiv \mu$, this is illustrated in Figure 4 for a constant value of the total slip $\sigma = \sigma^{\text{cr}}$, with $\sigma_x = \sigma_y > 0$, together with the plot of velocity field of Equation (41). The red circles represent the friction circle $\mathcal{C}_\mu$, whilst the dashed boundary is the locus of points for which the derivative of the Lyapunov function $V(\boldsymbol{F}_{\boldsymbol{t}}(t)) \triangleq \frac{1}{2} F_{\boldsymbol{t}}^2(t)$ vanishes. Basically, the inner regions enclosed by the dashed curves are invariant sets for $\boldsymbol{F}_{\boldsymbol{t}}(t)$, and, therefore, every circle that contains these regions is also an invariant set. It may be clearly noticed that, for very small values of the relaxation ratio ($\chi_\lambda = 0.125$), the dashed curve lies partially outside $\overset{\circ}{\mathcal{C}}_\mu$, and therefore the trajectories starting in $\overset{\circ}{\mathcal{C}}_\mu$ may happen to leave $\overset{\circ}{\mathcal{C}}_\mu$, implying $F_{\boldsymbol{t}}(t) \geq \mu F_z$ for some finite time t.

Other qualitative considerations may be drawn by looking at Figure 5, where the invariant sets are plotted for a tyre with relaxation ratio $\chi_\lambda = 0.125$ ($\lambda'_{\sigma_y} > \lambda'_{\sigma_x}$) for different directions θ of the critical slip value ($\sigma_x = \sigma^{\text{cr}} \cos\theta, \sigma_y = \sigma^{\text{cr}} \sin\theta$). In particular, it may be deduced that, when the slip is oriented in the same direction for which the relaxation length is larger, the invariant set becomes smaller and the risk of leaving $\overset{\circ}{\mathcal{C}}_\mu$ decreases. More specifically, Figure 5(d) is particularly interesting, since it shows that, when the slip has only lateral component, that is $\sigma_y = \sigma^{\text{cr}}$, the invariant set is completely contained within $\mathcal{C}_\mu$. Again, this is a consequence of the anisotropic nature of the tyre carcass.

In reality, the requirement on $\sup_{t \geq t_0} \sigma(t)$ imposed by Theorem 4.1 is quite stringent and might be relaxed if different maximum values are allowed depending on the slip direction. In fact, defining the Lyapunov function $V(\boldsymbol{F}_{\boldsymbol{t}}(t)) \triangleq \frac{1}{2} F_{\boldsymbol{t}}^2(t)$ as in Appendix 2, and assuming $C'_{\sigma_x} > C'_{\sigma_y}$ ($\lambda'_{\sigma_y} > \lambda'_{\sigma_x}$) as in common practice, it is possible to deduce immediately that any value of $\sigma(t)$ such that

$$\sigma(t) < \sigma_\chi^*\left(\theta(t)\right) \triangleq \sigma_\chi \frac{1}{\sqrt{\left(\cos\theta(t)\right)^2 + \left(\chi_\lambda \sin\theta(t)\right)^2}} \tag{47}$$

ensures that $\dot{V}(\boldsymbol{F}_{\boldsymbol{t}}(t))$ is negative definite at time t. From Equation (47), it may be inferred that, when $\sigma_x = \sigma \cos\theta(t) = 0$, the maximum slip in lateral direction coincides with the critical one (for $\epsilon \to 0^+$). *Vice versa*, when $\boldsymbol{\sigma}(t)$ has no lateral component, the maximum slip is again given by Equation (44) in Theorem 4.1. The fundamental conclusion is that, in transient conditions, the anisotropy of the tyre carcass maps the friction circle $\mathcal{C}_\mu$ into a *relaxation ellipse* $\mathcal{E}_\chi = \{\boldsymbol{F}_{\boldsymbol{t}} \in \mathbb{R}^2 \mid F_{\boldsymbol{t}} \leq \sigma_\epsilon^{-1}(\sigma_\chi^*(\theta); \epsilon)\}$. The relaxation set $\mathcal{C}_\chi$ may be then defined as the largest circle completely enclosed in $\mathcal{E}_\chi$, and $\sigma_\chi \equiv \sup_\theta \sigma_\chi^*(\theta)$, as illustrated graphically in Figure 6.

4.1.2. Dissipativity

Since the model is dynamic, there may be different phases in which energy is stored and released, alternatively. It may be proved that the map $\mathcal{X} : V_{\text{r}}\boldsymbol{\sigma} \mapsto \boldsymbol{F}_{\boldsymbol{t}}$ is dissipative for the model, and even more specifically passive .[3] This statement may be reformulated mathematically in the following Property 4.1.

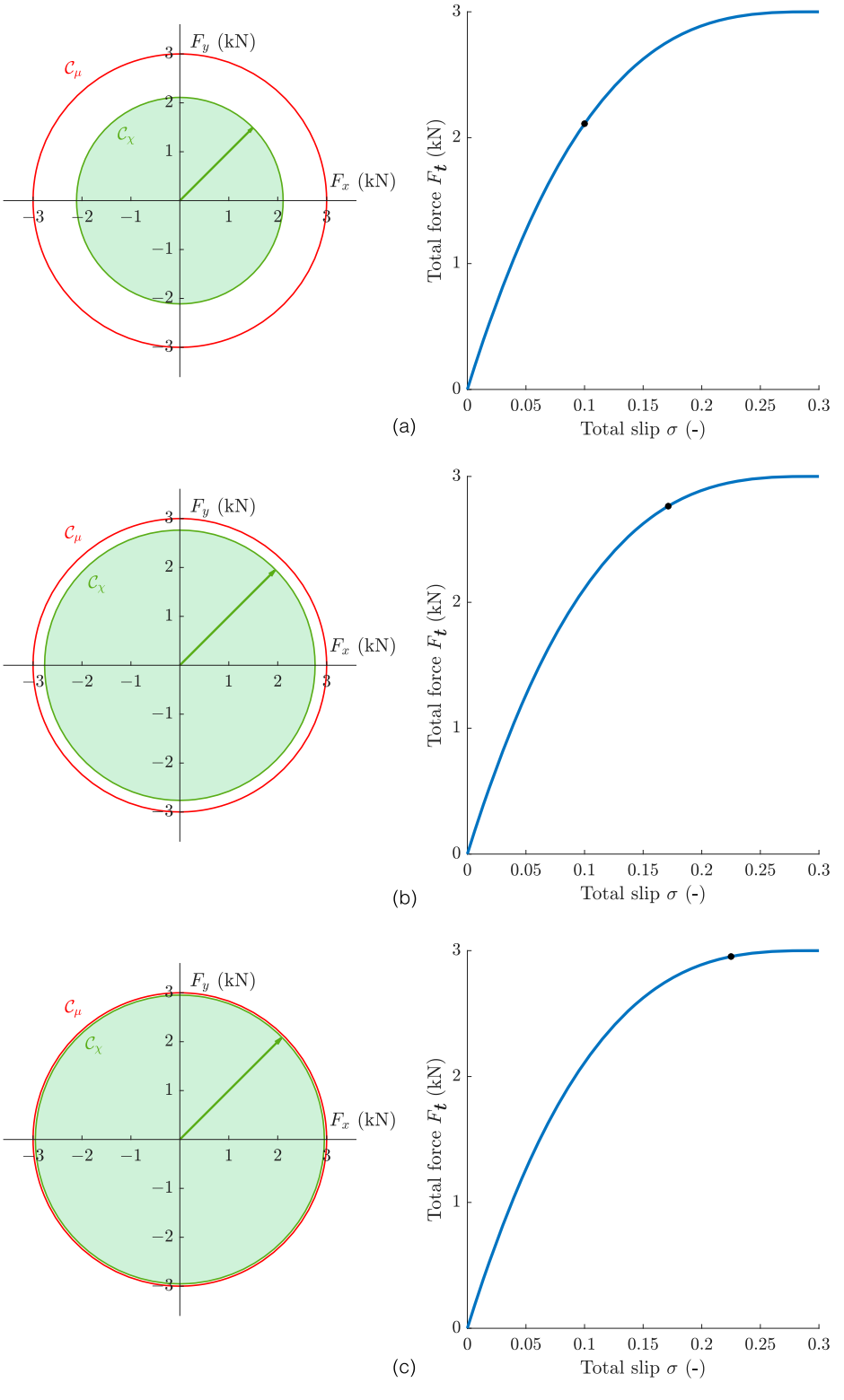

Figure 3. Friction circle and maximum attainable steady-state tangential force for a tyre with isotropic tread and anisotropic carcass with different relaxation ratios χ_λ: (a) $\chi_\lambda = 0.33$; (b) $\chi_\lambda = 0.57$; (c) $\chi_\lambda = 0.75$.

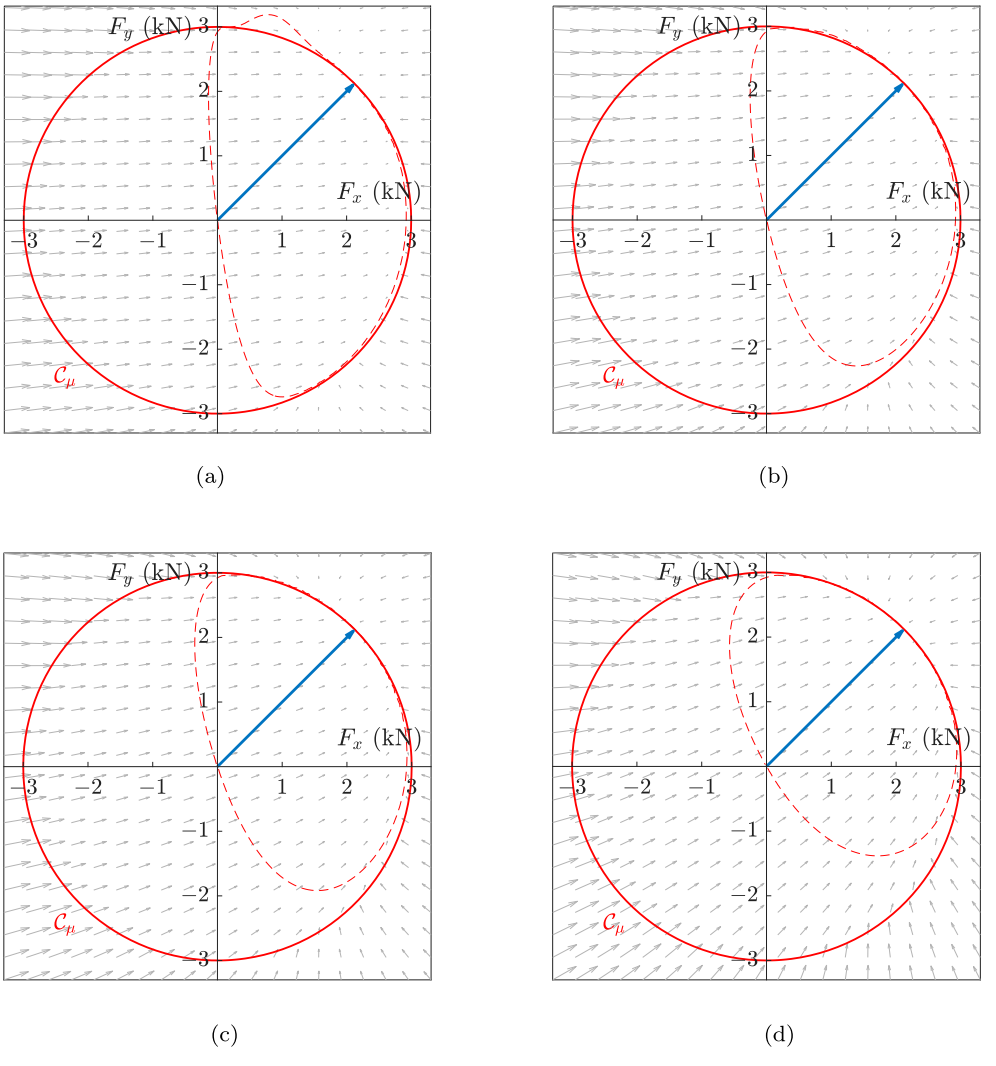

Figure 4. Velocity field and invariant sets for a tyre with isotropic tread and anisotropic carcass with different relaxation ratios χ_λ. $\sigma = \sigma^{\text{peak}} \equiv \sigma^{\text{cr}}$, $\sigma_x = \sigma_y > 0$: (a) $\chi_\lambda = 0.125$, (b) $\chi_\lambda = 0.25$, (c) $\chi_\lambda = 0.33$, (d) $\chi_\lambda = 0.57$.

Property 4.1 (Passivity): The map $\mathcal{X} : V_{\text{r}}\boldsymbol{\sigma} \mapsto \boldsymbol{F_t}$ is dissipative (passive) with respect to the storage function $V(\boldsymbol{F_t}(t)) \triangleq \frac{1}{2}\mathbf{S}'_{\boldsymbol{F}}\boldsymbol{F_t}(t) \cdot \boldsymbol{F_t}(t)$.

Proof: Recalling that $\mathbf{C}'_{\boldsymbol{\sigma}} \triangleq \mathbf{S}'^{-1}_{\boldsymbol{F}}$, it follows directly from Equation (41) that

$$\begin{aligned} V_{\text{r}}(t)\boldsymbol{\sigma}(t) \cdot \boldsymbol{F_t}(t) &= \mathbf{S}'_{\boldsymbol{F}}\dot{\boldsymbol{F}}_{\boldsymbol{t}}(t) \cdot \boldsymbol{F_t}(t) + V_{\text{r}}(t)\hat{\boldsymbol{\sigma}}_\epsilon\left(\boldsymbol{F_t}(t)\right) \cdot \boldsymbol{F_t}(t) \\ &\geq \mathbf{S}'_{\boldsymbol{F}}\dot{\boldsymbol{F}}_{\boldsymbol{t}}(t) \cdot \boldsymbol{F_t}(t) = \dot{V}\left(\boldsymbol{F_t}(t)\right). \end{aligned} \tag{48}$$

■

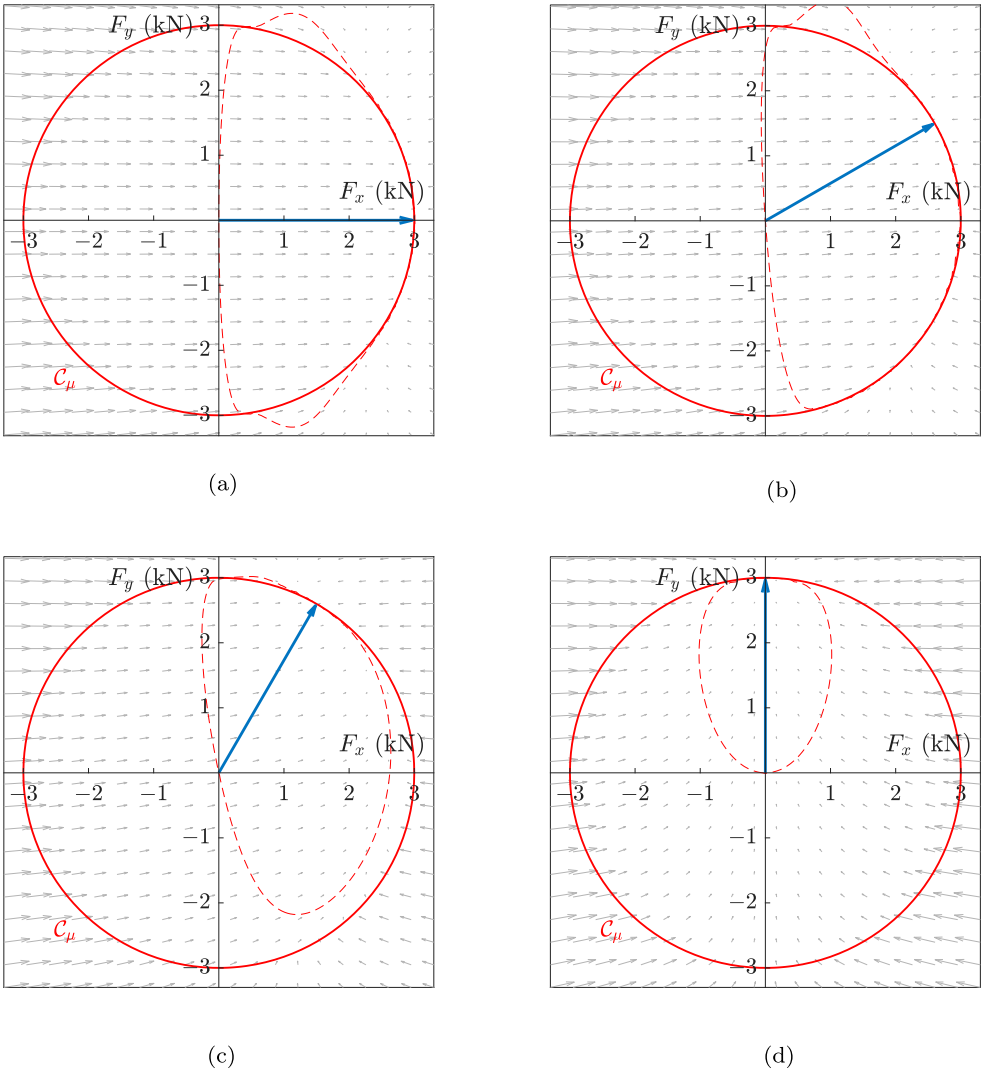

Figure 5. Velocity field and invariant sets for a tyre with low relaxation ratio $\chi_\lambda = 0.125$ for different values of the critical slip direction: (a) $\theta = 0°$, (b) $\theta = \frac{\pi}{6}$, (c) $\theta = \frac{\pi}{3}$, (d) $\theta = \frac{\pi}{2}$.

Since the storage function $V(\boldsymbol{F_t}(t))$ defined in Property 4.1 represents the elastic energy stored in the tyre carcass, the result above has a clear physical meaning: the power dissipated at the tyre contact patch is always greater than the variation in elastic energy accumulated in the tyre carcass. In particular, Equation (48) holds with strict inequality for any $\boldsymbol{F_t}(t) \neq \boldsymbol{0}$. From these considerations, it may be deduced that, in transient conditions, a finite slip input is not converted completely, and instantaneously, into tangential force, as it happens in the steady-state case. Therefore, the difference between $V_\tau(t)\boldsymbol{\sigma}(t) \cdot \boldsymbol{F_t}(t)$ and $\dot{V}(\boldsymbol{F_t}(t))$ may equivalently be interpreted as a power dissipation taking place inside the carcass. This might appear counter-intuitive at first instance, since the tyre carcass is modelled as an elastic element, and is due to the fact that, in transient conditions, the tyre

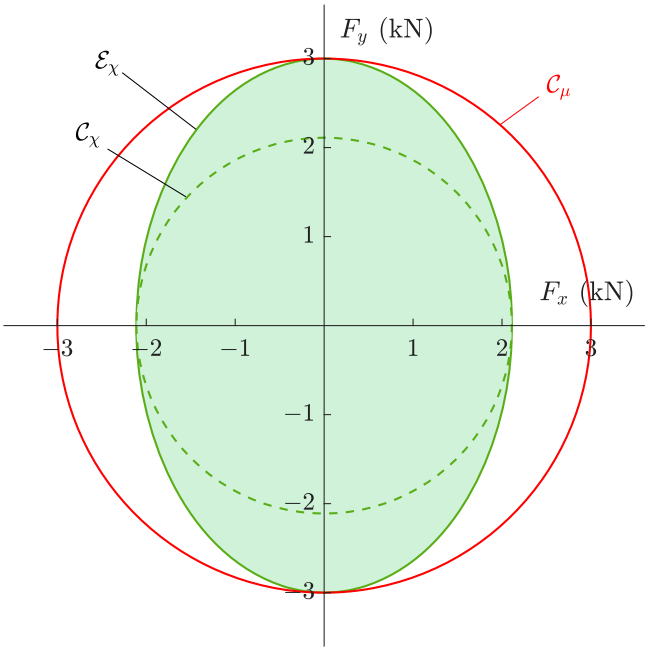

Figure 6. Friction circle $\mathcal{C}_\mu$ together with the relaxation ellipse $\mathcal{E}_\chi$ and the relaxation circle $\mathcal{C}_\chi$ for a tyre with isotropic tread and anisotropic carcass ($\chi_\lambda = 0.33$). The tyre carcass is stiffer in the longitudinal direction, that is $C'_x > C'_y$ and hence also $C'_{\sigma_x} > C'_{\sigma_y}$, $\lambda'_{\sigma_y} > \lambda'_{\sigma_x}$.

exhibits an intermediate behaviour between a linear spring and a damper. In this context, it is also worth remarking that, according to the global equilibrium approach, the quantity $V_{\mathrm{r}}(t)\boldsymbol{\sigma}(t) \cdot \boldsymbol{F_t}(t)$ also represents the total slip losses taking place inside the contact patch, at least in steady-state conditions.

5. Model comparison and validation

The present section addresses the validation of the two-regime tyre model.

5.1. Comparison with single contact point tyre models

The two-regime model developed in Section 4 is first compared versus the single contact points. The following investigation is conducted by only considering translational slips lower than σ_χ. The steady-state relationship for the tyre forces is chosen as in Equation (30). According to Assumption 3.1, the carcass stiffness matrix $\mathbf{C}'$ is assumed to be diagonal, but with different values for C'_x and C'_y. Finally, the travelled distance s defined in Section 4 is used as independent variable in place of the time t. By doing so, the problem under consideration becomes independent of the rolling speed. Owing to these premises, the following set of equations for the semi-nonlinear single point contact model may be introduced:

$$\boldsymbol{\Lambda}_{\boldsymbol{\sigma}} \frac{\mathrm{d}\boldsymbol{\sigma}'(s)}{\mathrm{d}s} + \boldsymbol{\sigma}'(s) = \boldsymbol{\sigma}(s), \tag{49a}$$

$$\boldsymbol{F_t}(s) = C_\sigma \boldsymbol{\sigma}'(s) \left[1 - \frac{\sigma'(s)}{\sigma^{\mathrm{cr}}} + \frac{1}{3} \left(\frac{\sigma'(s)}{\sigma^{\mathrm{cr}}} \right)^2 \right], \tag{49b}$$

where $\sigma'(s) = \left\| \boldsymbol{\nu}'(s) \right\|_2$ and the matrix $\Lambda_{\boldsymbol{\sigma}}$ reads specifically

$$\boldsymbol{\Lambda_\sigma} = \begin{bmatrix} \lambda_{\sigma_x} & 0 \\ 0 & \lambda_{\sigma_y} \end{bmatrix} = \begin{bmatrix} \dfrac{C_\sigma}{C'_x} & 0 \\ 0 & \dfrac{C_\sigma}{C'_y} \end{bmatrix}, \tag{50}$$

since $C_{x\sigma_y} = C_{y\sigma_x} = 0$. In Equation (50), it has been renamed $C'_x \triangleq C'_{xx}$, $C'_y \triangleq C'_{yy}$ and $\lambda_{\sigma_x} \triangleq \lambda_{x\sigma_x}$, $\lambda_{\sigma_y} \triangleq \lambda_{y\sigma_y}$ without ambiguity. The above system given by Equation (49a) combines a linear ODE (49a) for the transient slip $\boldsymbol{\sigma}'(s)$ and an algebraic Equation (49b) (although nonlinear) in $\boldsymbol{\sigma}'(s)$ for the planar force vector $\boldsymbol{F_t}(s)$. The second model is the full-nonlinear single contact point. The equations are as follows:

$$\tilde{\boldsymbol{\Lambda}}_{\boldsymbol{\sigma}} \left(\boldsymbol{\sigma}'(s) \right) \frac{\mathrm{d}\boldsymbol{\sigma}'(s)}{\mathrm{d}s} + \boldsymbol{\sigma}'(s) = \boldsymbol{\sigma}(s), \tag{51a}$$

$$\tilde{\boldsymbol{\Lambda}}_{\boldsymbol{\sigma}} \left(\boldsymbol{\sigma}'(s) \right) = \begin{bmatrix} \dfrac{\tilde{C}_{x\sigma_x}\left(\boldsymbol{\sigma}'(s) \right)}{C'_x} & \dfrac{\tilde{C}_{x\sigma_y}\left(\boldsymbol{\sigma}'(s) \right)}{C'_x} \\ \dfrac{\tilde{C}_{y\sigma_x}\left(\boldsymbol{\sigma}'(s) \right)}{C'_y} & \dfrac{\tilde{C}_{y\sigma_y}\left(\boldsymbol{\sigma}'(s) \right)}{C'_y} \end{bmatrix}, \tag{51b}$$

with

$$\tilde{C}_{x\sigma_x}\left(\boldsymbol{\sigma}'(s) \right) = \frac{\partial F_x\left(\boldsymbol{\sigma}'(s) \right)}{\partial \sigma'_x} = C_\sigma \left[1 - \frac{2\sigma'_x(s) + \sigma'_y(s)}{\sigma^{\mathrm{cr}}\sigma'(s)} + \left(\frac{\sigma'_x(s)}{\sigma^{\mathrm{cr}}} \right)^2 + \frac{1}{3} \left(\frac{\sigma'_y(s)}{\sigma^{\mathrm{cr}}} \right)^2 \right], \tag{52a}$$

$$\tilde{C}_{y\sigma_y}\left(\boldsymbol{\sigma}'(s) \right) = \frac{\partial F_y\left(\boldsymbol{\sigma}'(s) \right)}{\partial \sigma'_y} = C_\sigma \left[1 - \frac{2\sigma'_y(s) + \sigma'_x(s)}{\sigma^{\mathrm{cr}}\sigma'(s)} + \left(\frac{\sigma'_y(s)}{\sigma^{\mathrm{cr}}} \right)^2 + \frac{1}{3} \left(\frac{\sigma'_x(s)}{\sigma^{\mathrm{cr}}} \right)^2 \right], \tag{52b}$$

$$\begin{aligned} \tilde{C}_{x\sigma_y}\left(\boldsymbol{\sigma}'(s) \right) \equiv \tilde{C}_{y\sigma_x}\left(\boldsymbol{\sigma}'(s) \right) &= \frac{\partial F_x\left(\boldsymbol{\sigma}'(s) \right)}{\partial \sigma'_y} = \frac{\partial F_y\left(\boldsymbol{\sigma}'(s) \right)}{\partial \sigma'_x} \\ &= -C_\sigma \frac{\sigma'_x(s)\sigma'_y(s)}{\sigma^{\mathrm{cr}}} \left[\frac{1}{\sigma'(s)} - \frac{2}{3\sigma^{\mathrm{cr}}} \right]. \end{aligned} \tag{52c}$$

Equation (51a) together with Equations (51b) and (52a) are again used as input to Equation (49b). In this case, however, the ODE (51a) is highly nonlinear.

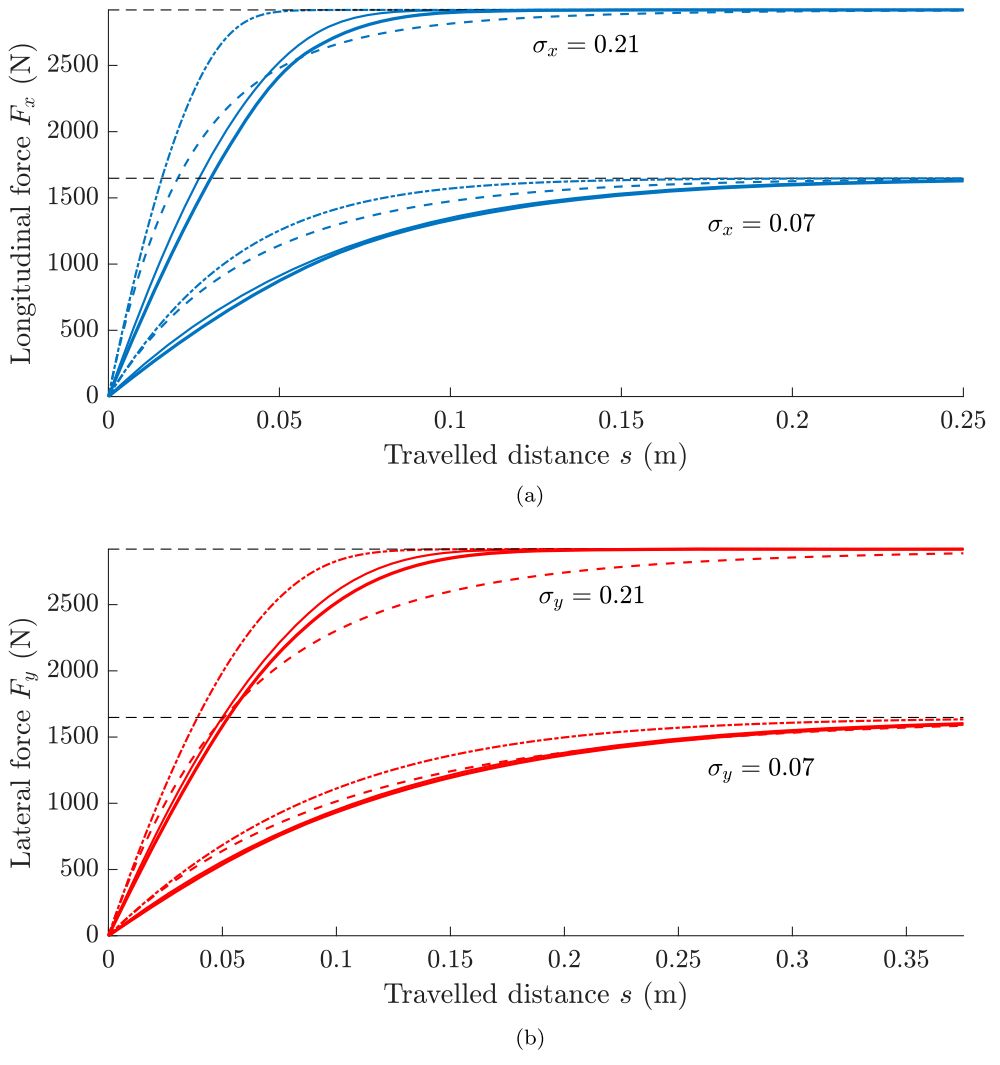

Figure 7. Comparison between the two-regime tyre model (solid line), the semi-nonlinear (dashed line), the full-nonlinear single point contact model (dash-dotted line) and Guiggiani's nonlinear full contact patch (thick line). Generally speaking, a better agreement between the two-regime model and the nonlinear full contact patch may be observed. (a) Simulation results for the two-regime tyre model (solid line), the semi-nonlinear (dashed line), the full-nonlinear single point contact model (dash-dotted line) and Guiggiani's nonlinear full contact patch (thick line) for different value of the longitudinal slip input $\sigma_x = 0.07$ and $\sigma_x = 0.21$. (b) Simulation results for the two-regime tyre model (solid line), the semi-nonlinear (dashed line), the full-nonlinear single point contact model (dash-dotted line) and Guiggiani's nonlinear full contact patch (thick line) for different value of the lateral slip input $\sigma_y = 0.07$ and $\sigma_y = 0.21$.

The two-regime model is instead formulated directly in state–space form. With the travelled distance as independent variable, the system in Equation (41) becomes

$$\frac{\mathrm{d}\boldsymbol{F_t}(s)}{\mathrm{d}s} = \mathbf{C}'_{\boldsymbol{\sigma}} \left[\boldsymbol{\sigma}(s) - \hat{\boldsymbol{\sigma}}_{\epsilon} \left(\boldsymbol{F_t}(s); \epsilon \right) \right], \tag{53}$$

Table 1. Tyre parameters.

Parameter	Description	Unit	Value
C_σ	Slip stiffness	N	$3 \cdot 10^4$
C'_x	Longitudinal stiffness of the carcass	N m^{-1}	$6 \cdot 10^5$
C'_y	Lateral stiffness of the carcass	N m^{-1}	$2.4 \cdot 10^5$
F_z	Vertical force	N	3000
a	Contact patch semilength	m	0.075
μ	Friction coefficient	–	1

where the matrix $\mathbf{C}'_{\boldsymbol{\sigma}}$ is defined as in Equation (37) and the slip function $\hat{\boldsymbol{\sigma}}(\cdot)$ in Equation (31) is replaced more conveniently by $\hat{\boldsymbol{\sigma}}_\epsilon(\cdot;\epsilon)$.

A first set of simulations is aimed at comparing the three approximated models given by Equations (49), (53) and (51) with the exact solution to Equation (1) starting from an initial undeformed configuration and subjected to the constraint imposed by Equation (5) (Guiggiani's nonlinear full contact patch model [1]). The equations for the complete model are derived in Guiggiani's book [1] and are not reported here for brevity. Furthermore, for the sake of simplicity, the longitudinal and lateral problems are analysed in isolation in Figure 7. Indeed, even in the case of pure longitudinal or lateral interactions, Equation (1) does not admit a closed-form solution and need to be solved numerically[4]. Generally, it may be observed that the two-regime model succeeds better in replicating the exact trend, whereas the single contact point models exhibit larger discrepancies especially at higher values of the slip inputs. The parameters for the simulation are listed in Table 1.

A second comparison between the three approximated models is shown for different combinations of constant slip inputs σ_x and σ_y in Figure 8. The slip value is set to $\sigma = 0.17 < \sigma_\chi$. It may be noticed that the agreement between the two-regime tyre model and the semi-nonlinear single contact point is particularly good in the beginning, when the forces are in the linear region of the diagram $\boldsymbol{F_t} - \boldsymbol{\sigma}$ and the assumption of constant relaxation length holds fairly. As the travelled distance increases and the tyre characteristics develop fully, the two-regime transient model exhibits a faster convergence to the steady-state solution, and tends to the full-nonlinear one. Clearly, all the models converge in any case to the same asymptotic value.

Finally, a third set of simulation, whose results are shown in Figure 9, is carried out to illustrate the models behaviour when the tyres are subjected to a sinusoidal forcing term modelled as $\boldsymbol{\sigma}(s) = \bar{\boldsymbol{\sigma}}[0.9 + 0.1\sin(\omega s)]$. For both excitation frequencies, $\omega = 10\pi$ and 50π, the slip amplitudes are limited to $\bar{\sigma}_x = \bar{\sigma}_y = 0.12$. Generally speaking, there is again a very encouraging match between the two-regime tyre transient and the full-nonlinear one, whilst the discrepancy with the semi-nonlinear single contact point is due to the approximation of constant relaxation length.

5.2. Comparison with experimental data

In this paper, the transient response of the tyre predicted using the two-regime model was partially validated against a series of consecutive deceleration manoeuvres. To the purpose of experimental validation, two different braking tests were considered in turn: Test 1 was characterised by a sequence of relatively small, continuously time-varying slips inputs (up to $|\sigma_x| = 0.3$), whilst Test 2 was aimed at stressing the tyre up to the saturated region of

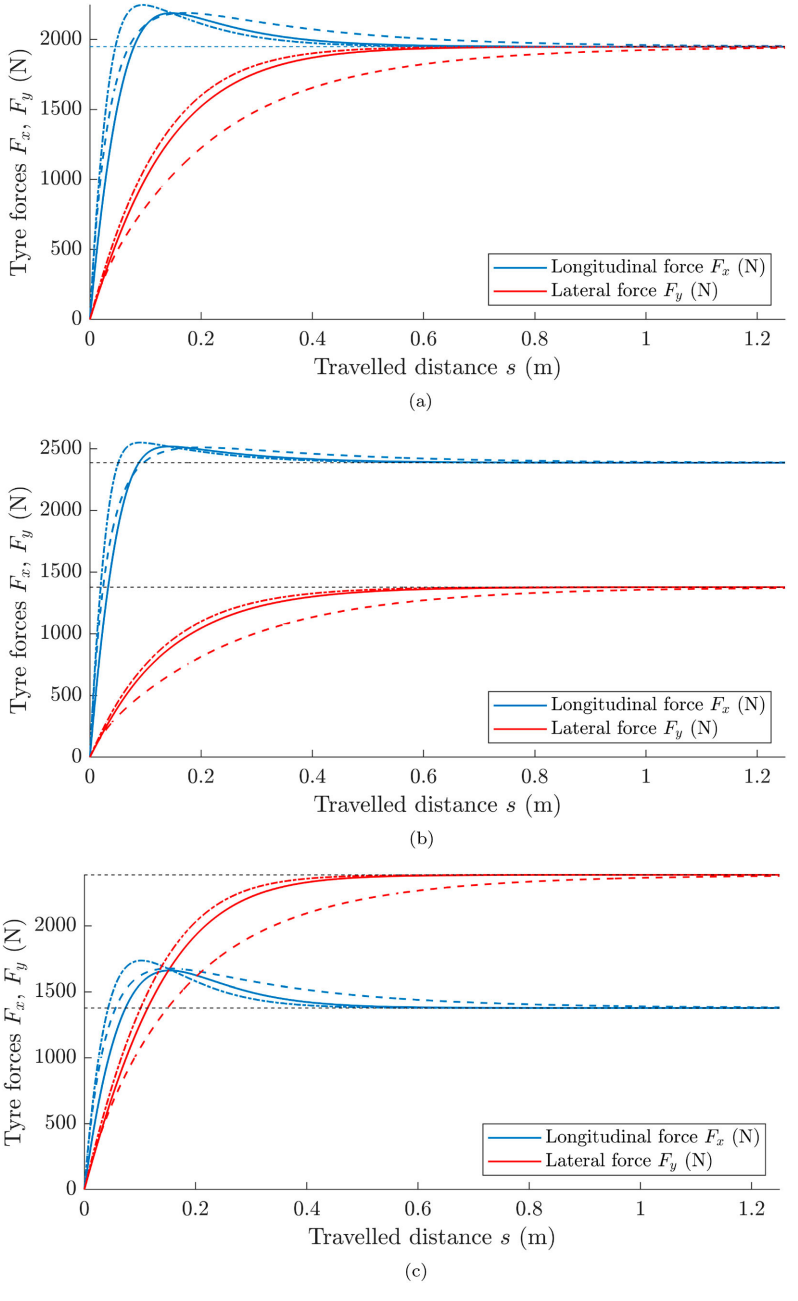

Figure 8. Comparison between the two-regime tyre model (solid line), the semi-nonlinear (dashed line) and the full-nonlinear single point contact model (dash-dotted line) for different longitudinal and lateral slip inputs σ_x and σ_y, respectively. It may be noticed a better agreement between the first two models for low values of the slip force, where the approximation of constant relaxation length holds for both formulations. Conversely, as the value of the force increases, the two-regime tyre model exhibits a similar behaviour to the full-nonlinear single contact point one. The black dashed line represent the steady-state values for the longitudinal and tangential forces. (a) Slip inputs: $\sigma_x = \sigma_y = 0.12$. (b) Slip inputs: $\sigma_x = 0.085$, $\sigma_y = 0.14$. (c) Slip inputs: $\sigma_x = 0.14$, $\sigma_y = 0.085$.

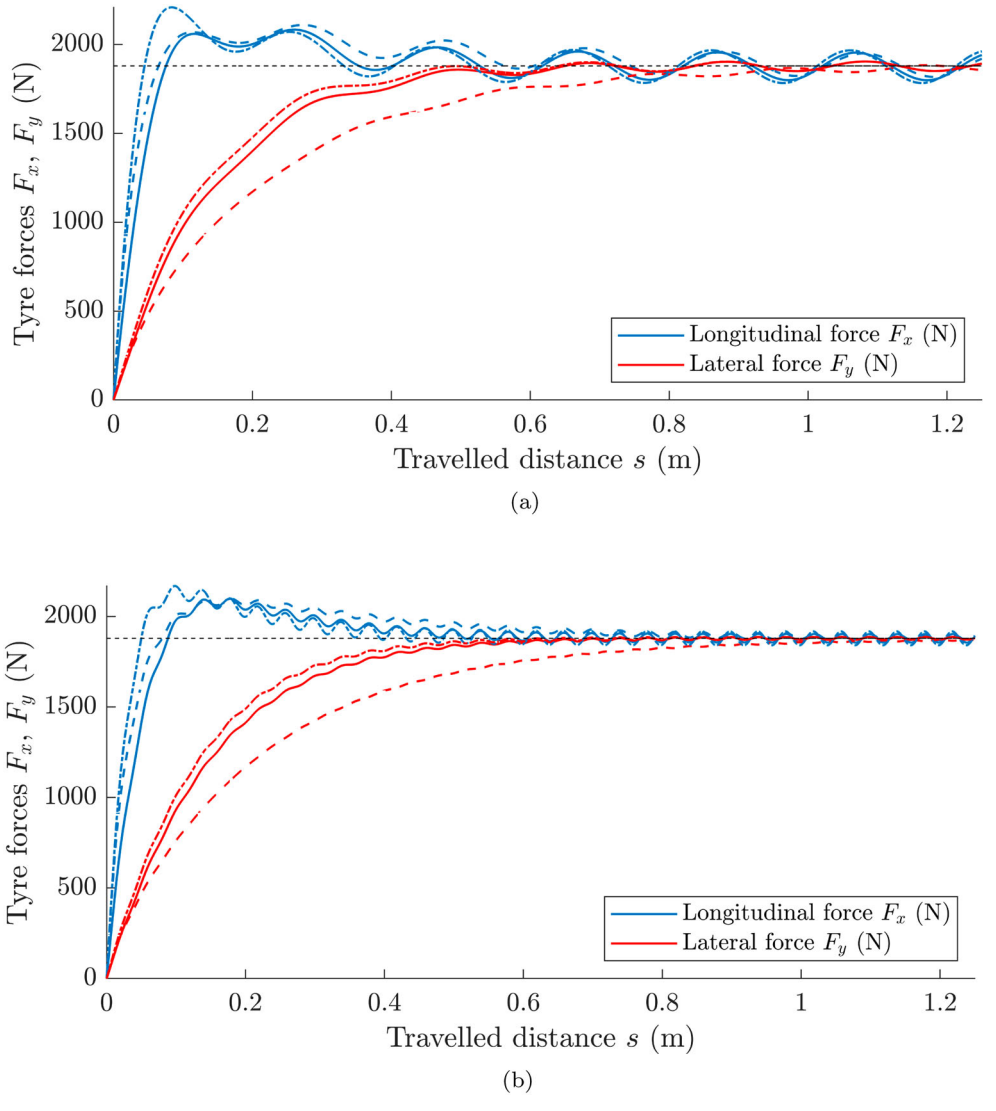

Figure 9. Comparison between the two-regime tyre model (solid line), the semi-nonlinear (dashed line) and the full-nonlinear single point contact model (dash-dotted line) for different excitation frequencies ω. It may be noticed that both the two-regime and the full-nonlinear single contact point models succeed in following the oscillatory trend of the input, whilst the lateral tyre characteristic predicted by the semi-nonlinear model seem to be almost unaffected by the harmonic component of the forcing term. (a) Slip amplitude: $\bar{\sigma}_x = \bar{\sigma}_y = 0.12$; excitation frequency $\omega = 10\pi$ m^{-1}. (b) Slip amplitude: $\bar{\sigma}_x = \bar{\sigma}_y = 0.12$; excitation frequency $\omega = 50\pi$ m^{-1}.

the slip curve. Both tests involved the VTI friction test vehicle BV12 shown in Figure 10: a specially equipped truck with a test wheel suspension for passenger car wheels (in the following example, the wheel mounted a 4 D1 Continental/Ice Contact 2 tyre, with a nominal radius of 0.36 m).

Figure 10. The VTI friction test vehicle BV12.

Some peculiar features of the BV12 are as follows. The test wheel can be forced to rotate at the constant slip that produces maximum braking performance by means of a cardan shaft connected to a gearbox with continuously variable slip. The wheel can also be locked by means of a disk brake after being decoupled from the gearbox. The braking force is calculated from wheel torque, which is measured by a transducer on the cardan shaft to the wheel. The wheel load is obtained by means of dead weights acting on a spring/damper. Furthermore, wheel rotational velocity and travelled distance are measured. From these values, the longitudinal slip σ_x and rolling radius can be easily calculated.

Data collected during Test 1 were specifically employed to parametrise the transient longitudinal model according to the two-regime formulation of Equation (41) (again with $\hat{\boldsymbol{\sigma}}(\cdot)$ in Equation (31) modified as $\hat{\boldsymbol{\sigma}}_\epsilon(\cdot;\epsilon)$), whilst Test 2 was mainly used for validation. In this regard, it is worth emphasising that, due to the intrinsic nature of the tests considered in the paper, only the pure longitudinal transient behaviour of the tyre could be validated. Moreover, since the longitudinal dynamics was considered in isolation and the influence of the lateral slip was systematically disregarded, the transient critical slip σ_χ was fairly assumed to be coincident with the corresponding steady-state value, i.e. $\sigma_\chi \equiv \sigma^{\mathrm{cr}}$.

For both tests, large variation in the normal force acting on the tyre could also be observed during the braking phases. To cope with this aspect, the explicit dependence upon the vertical load acting on the tyre was also taken into account in the parametrisation and validation processes. In particular, a simple linear model for the slip stiffness C_σ as a function of F_z was assumed in this paper of the type $C_\sigma = \bar{C}_\sigma F_z$. Starting from

the relationship $C_\sigma = 4a^2bk$, the contact patch semilength was derived to be dependent upon F_z as $a = \bar{a}\sqrt{\bar{C}_\sigma F_z}$, with $\bar{a} = 1/\sqrt{4bk}$. For the sake of simplicity, the semiwidth b was instead assumed to be constant over time. According to the brush theory, the critical slip value was also modelled explicitly as a function of the friction coefficient μ as $\sigma^{\mathrm{cr}} = 3\mu F_z/C_\sigma \equiv 3\mu/\bar{C}_\sigma$. Therefore, defining the longitudinal friction as $\mu_x \triangleq F_x/F_z$ and $\hat{\mu}_x(\cdot) \triangleq \hat{F}_x(\cdot)/F_z$, it was possible to restate the longitudinal component of Equation (30) as

$$\mu_x = \hat{\mu}_x(\sigma_x) = \bar{C}_\sigma \sigma_x \left[1 - \bar{C}_\sigma \frac{|\sigma_x|}{3\mu} + \frac{1}{3}\left(\bar{C}_\sigma \frac{\sigma_x}{3\mu}\right)^2\right], \quad \sigma_x \in (-3\mu/\bar{C}_\sigma, 3\mu/\bar{C}_\sigma). \quad (54)$$

Owing to these premises, the tyre model was parameterised in a two-step process: first, initial values for the structural parameter $\bar{C}_\sigma$ and the friction coefficient μ in Equation (54) were estimated employing an iterative procedure based on the least-square

Table 2. Tyre parameters optimised from experimental data.

Parameter	Description	Unit	Value
$\bar{C}_\sigma$	Normalised slip stiffness	–	7.6
μ	Friction coefficient	–	0.48
C'_x	Lateral stiffness of the carcass	$\mathrm{N\,m^{-1}}$	$8.61 \cdot 10^5$
$\bar{a}$	Contact patch parameter	$\mathrm{m\,N^{-1/2}}$	0.0003

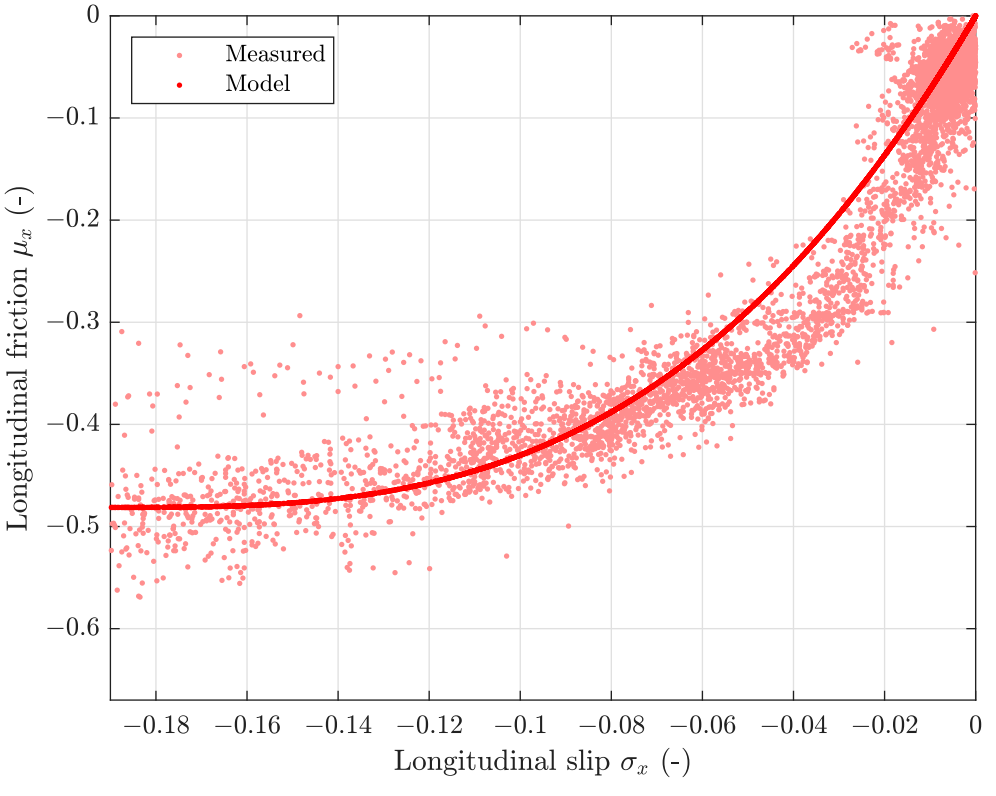

Figure 11. Tyre-slip curve fitted from experimental data. Parameter values: $\bar{C}_\sigma = 7.6$, $\mu = 0.48$.

fitting technique. Specifically, these quantities were optimised restricting the attention to the nonlinear region of the tyre-slip curve in the range $\sigma_x \in (-\sigma^{\mathrm{cr}}, -\sigma^{\mathrm{cr}}/3] = (-3\mu/\bar{C}_\sigma, -\mu/\bar{C}_\sigma]$, where the transient dynamics of the tyre was expected to play a minor role due to the fast excitation caused by large longitudinal slips (slip was defined with negative sign for braking). Since $\bar{C}_\sigma$ and μ were also unknown, the procedure was iterated multiple times until convergence to ensure that only the desired points were included when optimising both parameters. At each iteration, the previous estimate for σ^{cr} was used to select the appropriate samples. The normalised slip stiffness was constrained between $0 \leq \bar{C}_\sigma \leq 10$, whilst lower and upper bounds for the friction coefficient were specified as $0 \leq \mu \leq 0.6$. The upper limit on μ was motivated by the fact that the maximum observed ratio μ_x between the longitudinal tyre force and the normal load was around 0.62 (as already pointed out, in the brush model the peak force equals μF_z, and therefore the maximum value for μ_x in Equation (30) is $\mu_{\mathrm{peak}} \equiv \mu$). For both quantities, the optimised values are reported in Table 2, whereas a comparison between the measured data points and the predicted steady-state behaviour of the tyre is shown graphically in Figure 11.

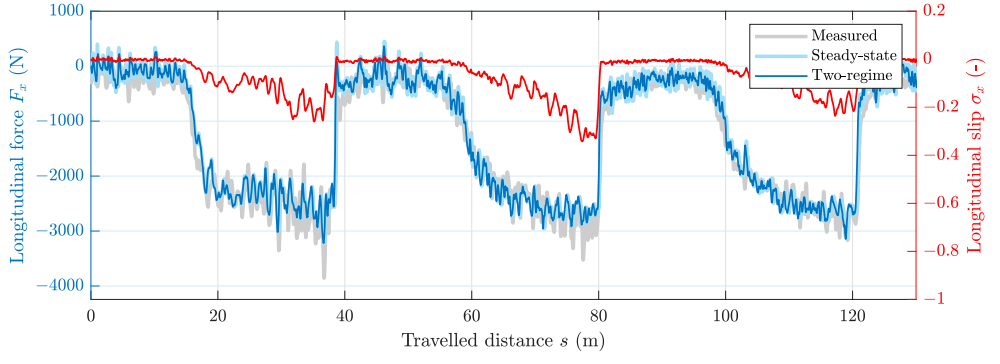

(a)

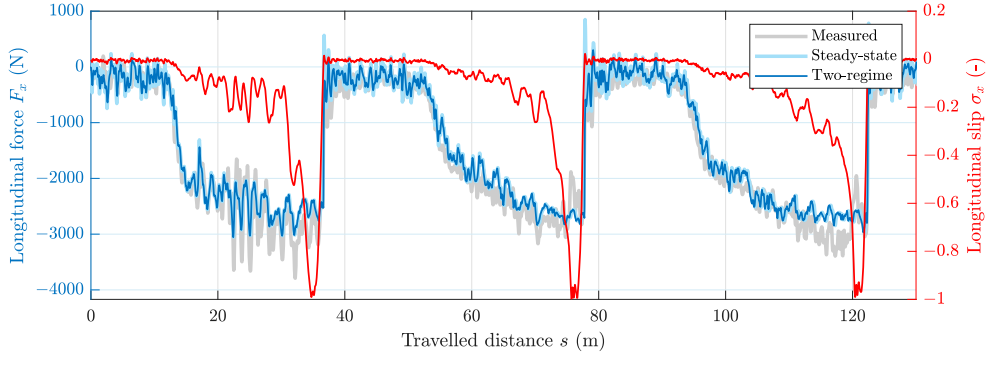

(b)

Figure 12. Transient longitudinal response of the tyre to a time-varying slip input σ_x (red line) predicted according to the two-regime model (blue line) and the steady-state Equation (54) (cyan line). The comparison is performed against the measured tyre force (grey line). (a) Transient longitudinal tyre response during Test 1. (b) Transient longitudinal tyre response during Test 2.

In a second step, the optimal values for the tyre carcass stiffness C'_x and the quantity $\bar{a}$ were found by minimising the error between the transient simulation results and the measured tyre data, using the travelled distance s as independent variable. In this process, the dynamic model described by Equation (41) was implemented by saturating the output $F_x(s)$, which was always constrained below the friction limit $\mu F_z(s)$. The dynamical system was then re-initialised to the measured longitudinal force every time that the latter fell below the estimated peak force. Again, the values extracted from the optimisation routine are listed in Table 2. A comparison between the transient behaviour predicted by the two-regime model (blue line), the steady-state Equation (54) (cyan line) and the experimental data (grey line) is shown in Figure 12 for both Test 1 and Test 2. Obviously, the match is far from being perfect due to the simplistic nature of the brush model, but a good qualitative agreement towards the measured tyre force may be observed overall, thus corroborating the potential of the proposed formulation. It should be noticed that the steady-state model for the longitudinal tyre force given by Equation (54) yields very similar results to the transient one, especially during severe braking phases, whereas larger discrepancies may be observed for relatively low values of the slip (in magnitude), where the slower dynamics of the two-regime formulation better matches the experimental results. The calculated root mean square errors (RMS) for the steady-state and transient models were 368.14 and 356.40 for Test 1 and 329.57 and 329.48 for Test 2, respectively.

6. Conclusion

In this paper, the two-regime theory recently introduced by Romano et al. [5] has been refined. First, a complete set of relationships – renamed *sliding functions* – existing between the slip variables and the tyre forces and moment at low rolling speeds has been derived. The notion of *slip functions* has also been introduced to formalise mathematically the corresponding steady-state relationships.

Second, a class of nonlinear dynamic models for combined translational slips has been developed that allows to describe the transient generation of tyre forces in a relatively simple way. The model generalises further the one presented in [5] and allows to circumvent the need to solve the complicated PDEs governing the tyre dynamics.

A formal analysis has been then conducted in Section 4 by resorting to the well-established theory for nonlinear systems. The investigation has been restricted to the case in which the steady-state tyre forces and the translational slips have the same direction. In this context, an estimate σ_χ on the supremum of the transient slip that always ensures partial adhesion in the contact patch has been provided. Indeed, any value $\sigma < \sigma_\chi$ implies automatically that the tyre forces never exploit the maximum friction available. The tyre carcass anisotropy plays a pivotal role in the determination of the parameter σ_χ through the relaxation ratio χ_λ. This is defined mathematically as the ratio between the smallest and largest eigenvalues of the enhanced stiffness matrix. For a tyre with a diagonal matrix for the carcass stiffnesses, this also coincides with the ratio between the minimum and maximum enhanced relaxation lengths. In transient conditions, low values of χ_λ correspond to smaller admissible slip inputs σ_χ compared to the critical slip value σ^{cr} that guarantees adhesion in steady-state conditions. This result may be exploited for control or optimisation purposes.

Then the focus has been shifted towards the physical properties of the new model. It has been demonstrated that the dynamical system used to describe the transient forces

dissipates power at the tyre–road interface. As a consequence, the frictional power generated due to finite slip is not stored completely in the elastic carcass.

Finally, in Section 5 the validation of the two-regime model introduced in this paper has been addressed. Specifically, in Section 5.1, the complete two-regime model for combined slip has been compared against the semi-nonlinear and the full-nonlinear single contact point models, and partially against Guiggiani's nonlinear full contact patch. The agreement between the first two formulations is especially good at a low value of the slip inputs, where the approximation of constant relaxation lengths holds fairly; as the slips increase, the two-regime transient model matches the full-nonlinear one. On the other hand, it has been also demonstrated that the two-regime model exhibits a better agreement to Guiggiani's complete model compared to the single contact points. The two-regime tyre models and the single contact point represent an approximation of the pure brush and the brush-string models, respectively. In the former, the tyre carcass is modelled using a linear spring, whilst the latter is based on a distributed description whose governing differential equations are the ones of a stretched string. Simulation results seem to suggest that the specific constitutive relationship chosen to model the carcass extensibility does not play a fundamental role for accurate prediction of the transient generation of forces and moment, since the two models behave very similarly. Additionally, the transient longitudinal dynamics of the tyre according to the two-regime formulation has been validated in isolation against experimental data in Section 5.2. In spite of the simplistic nature of the brush models, the behaviour predicted using the two-regime theory appears to agree qualitatively with the measured quantities, confirming the potential of the approach outlined in the paper.

Compared to the single contact point models, the two-regime model is simpler to implement and is more general from a theoretical viewpoint, since it considers the transient due to the bristle deflection. However, a closed-form expression for the two-regime formulation has only been possible to derive for the case of isotropic tread, whilst the single contact point models can use the transient slip as input to any tyre equation. The possibility of extending the two-regime theory to account for the tyre tread anisotropy must be therefore explored in future studies.

Forces and moments	**Unit**	**Description**
$\boldsymbol{F_t}$	N	Planar force vector
$\boldsymbol{F_{t0}}$	N	Initial conditions for the planar force vector
F_x, F_y	N	Longitudinal and lateral tyre forces
F_{x0}, F_{y0}	N	Initial conditions for the longitudinal and lateral tyre forces
F_z	N	Vertical force
M_z	N m	Self-aligning moment
$\boldsymbol{q_t}$	$\mathrm{N\,m^{-2}}$	Tangential shear stress vector
q_t	$\mathrm{N\,m^{-2}}$	Total tangential shear stress
q_x, q_y	$\mathrm{N\,m^{-2}}$	Longitudinal and lateral shear stress
q_z	$\mathrm{N\,m^{-2}}$	Vertical pressure
Displacements	**Unit**	**Description**
$\boldsymbol{u_t}$	m	Displacement vector of the bristle

u_x, u_y	m	Longitudinal and lateral displacement of the bristle
$\boldsymbol{u}_{t0}$	m	Initial tangential displacement vector of the bristle (IC)
u_{x0}, u_{y0}	m	Initial longitudinal and lateral displacement (IC)
s	m	Travelled distance
$\boldsymbol{x}$	m	Coordinate vector
x, y	m	Longitudinal and lateral coordinates
$\boldsymbol{\delta_t}$	m	Tyre carcass tangential displacement vector
δ_x, δ_y	m	Tyre carcass longitudinal and lateral displacements
Speeds	**Unit**	**Description**
V_r	$\mathrm{m\,s^{-1}}$	Rolling speed
$\boldsymbol{v_t}$	$\mathrm{m\,s^{-1}}$	Tangential velocity field
v_x, v_y	$\mathrm{m\,s^{-1}}$	Longitudinal and lateral components of the velocity field
$\boldsymbol{v}_\mathrm{s}$	$\mathrm{m\,s^{-1}}$	Micro-sliding velocity
$v_{\mathrm{s}x}$, $v_{\mathrm{s}y}$	$\mathrm{m\,s^{-1}}$	Longitudinal and lateral micro-sliding speeds
Slip Parameters	**Unit**	**Description**
$\boldsymbol{\sigma}$	–	Translational slip vector
σ	–	Total translational slip
σ_x, σ_y	–	Longitudinal and lateral slip
σ^cr	–	Global critical slip
σ_χ	–	Transient critical slip
$\boldsymbol{\sigma}'$	–	Transient slip vector
σ'	–	Total transient slip
σ'_x, σ'_y	–	Transient longitudinal and lateral slip
φ	$\mathrm{m^{-1}}$	Rotational slip or spin parameter
Rotation matrices and tensors	**Unit**	**Description**
$\mathbf{A}_\varphi$	$\mathrm{m^{-1}}$	Spin tensor
Geometric parameters	**Unit**	**Description**
a, b	m	Contact patch semilength and semiwidth
$\bar{a}$	$\mathrm{m\,N^{-1/2}}$	Contact patch parameter
R_r	m	Rolling radius
Λ	m	Matrix of relaxation lengths
$\tilde{\Lambda}_{\boldsymbol{\sigma}}$	m	Matrix of generalised relaxation lengths
$\Lambda'_{\boldsymbol{\sigma}}$	m	Matrix of enhanced relaxation lengths
$\lambda_{x\sigma_x}$, $\lambda_{y\sigma_y}$	m	Longitudinal and lateral relaxation length
$\lambda_{x\sigma_y}$, $\lambda_{y\sigma_x}$	m	Cross relaxation lengths
$\tilde{\lambda}_{x\sigma_x}$, $\tilde{\lambda}_{y\sigma_y}$	m	Generalised longitudinal and lateral relaxation length
$\tilde{\lambda}_{y\sigma_x}$, $\tilde{\lambda}_{x\sigma_y}$	m	Generalised cross relaxation lengths
$\lambda'_{x\sigma_x}$, $\lambda'_{y\sigma_y}$	m	Enhanced longitudinal and lateral relaxation length
λ'_max, λ'_min	m	Maximum and minimum enhanced relaxation length
χ_λ	–	Relaxation ratio

Stiffnesses and compliances	Unit	Description
$\mathbf{K}_{\boldsymbol{t}}$	$\mathrm{N\,m^{-3}}$	Matrix of the bristle tangential stiffnesses
k_{xx}, k_{yy}	$\mathrm{N\,m^{-3}}$	Longitudinal and lateral stiffness of the tread bristle
k_{xy}, k_{yx}	$\mathrm{N\,m^{-3}}$	Cross stiffnesses of the tread bristle
$\mathbf{C}_{\boldsymbol{\sigma}}$	N	Matrix of slip stiffnesses
$\tilde{\mathbf{C}}_{\boldsymbol{\sigma}}$	N	Matrix of generalised slip stiffnesses
$\mathbf{C}'_{\boldsymbol{\sigma}}$	$\mathrm{N\,m^{-1}}$	Enhanced matrix of slip stiffnesses
$C_{x\sigma_x}$, $C_{y\sigma_y}$	N	Longitudinal and lateral slip stiffnesses
$\tilde{C}_{x\sigma_x}$, $\tilde{C}_{y\sigma_y}$	N	Generalised longitudinal and lateral slip stiffnesses
$C'_{x\sigma_x}$, $C'_{y\sigma_y}$	$\mathrm{N\,m^{-1}}$	Enhanced longitudinal and lateral slip stiffnesses
$C_{x\sigma_y}$, $C_{y\sigma_x}$	N	Cross slip stiffnesses
$\tilde{C}_{x\sigma_y}$, $\tilde{C}_{y\sigma_x}$	N	Generalised cross slip stiffnesses
$C'_{x\sigma_y}$, $C'_{y\sigma_x}$	$\mathrm{N\,m^{-1}}$	Enhanced longitudinal and lateral cross slip stiffnesses
C_σ	N	Slip stiffness
$\bar{C}_\sigma$	–	Normalised slip stiffness
$C'_{\max} = C'_{\min}$	$\mathrm{N\,m^{-1}}$	Maximum and minimum enhanced stiffness
$\mathbf{C}'$	$\mathrm{N\,m^{-1}}$	Matrix of tyre carcass stiffnesses
C'_{xx}, C'_{yy}	$\mathrm{N\,m^{-1}}$	Longitudinal and lateral stiffness of the tyre carcass
C'_{xy}, C'_{yx}	$\mathrm{N\,m^{-1}}$	Cross stiffnesses of the tyre carcass
$\mathbf{S}'$	$\mathrm{m\,N^{-1}}$	Matrix of tyre carcass compliances
S'_{xx}, S'_{yy}	$\mathrm{m\,N^{-1}}$	Longitudinal and lateral compliance of the tyre carcass
S'_{xy}, S'_{yx}	$\mathrm{m\,N^{-1}}$	Cross compliances of the tyre carcass

Friction parameters	Unit	Description
μ	–	Friction coefficient
μ_{peak}	–	Peak friction coefficient
μ_x	–	Normalised longitudinal force

Functions and operators	Unit	Description
$\nabla_{\boldsymbol{t}}$	$\mathrm{m^{-1}}$	Tangential gradient
$\breve{\boldsymbol{\sigma}}(\cdot,\cdot)$, $\breve{\varphi}(\cdot,\cdot)$	-, $\mathrm{m^{-1}}$	Sliding functions
$\hat{\boldsymbol{\sigma}}(\cdot,\cdot)$, $\hat{\varphi}(\cdot,\cdot)$	-, $\mathrm{m^{-1}}$	Slip functions
$\hat{\boldsymbol{\sigma}}_\epsilon(\cdot;\cdot)$	–	Modified slip functions

Sets	Unit	Description
$\mathcal{C}\mu$	$\mathrm{N^2}$	Friction circle
$\overset{\circ}{\mathcal{C}}\mu$	$\mathrm{N^2}$	Interior of the friction circle
$\mathcal{C}\chi$	$\mathrm{N^2}$	Relaxation circle
$\overset{\circ}{\mathcal{C}}\chi$	$\mathrm{N^2}$	Interior of the relaxation circle
$\mathcal{E}\chi$	$\mathrm{N^2}$	Relaxation ellipse
$\overset{\circ}{\mathcal{E}}\chi$	$\mathrm{N^2}$	Interior of the relaxation ellipse
$\mathscr{P}$	$\mathrm{m^2}$	Contact patch
$\overset{\circ}{\mathscr{P}}$	$\mathrm{m^2}$	Interior of $\mathscr{P}$
$\partial\mathscr{P}$	m	Boundary of $\mathscr{P}$
$\mathscr{L}$	m	Leading edge

$\mathscr{N}$	m	Neutral edge
$\mathscr{T}$	m	Trailing edge
$\mathbb{R}_{\geq 0}$	–	Set of positive real numbers (including 0)
$\mathbb{R}_{>0}$	–	Set of strictly positive real numbers (excluding 0)

Notes

1. For example, Pacejka's Magic Formula.
2. For a definition of input-to-state stability, the reader is referred to Khalil [45] (Chapter 4).
3. For a mathematical definition of passivity, the reader is again redirected to Khalil [45, Chapter 6].
4. For example, using Euler's forward scheme.

Acknowledgments

The authors gratefully acknowledge financial support from the COVER project (44929-1), funded by the Swedish energy agency and the Swedish vehicle research and innovation program (FFI).

Disclosure statement

The authors declare that they have no conflict of interest.

Funding

The authors gratefully acknowledge financial support from the COVER project (44929-1), funded by the Swedish energy agency and the Swedish vehicle research and innovation program (FFI)

ORCID

Luigi Romano http://orcid.org/0000-0001-8435-7696
Bengt Jacobson http://orcid.org/0000-0002-5798-5651

References

[1] Guiggiani M. The science of vehicle dynamics. 2nd ed. Cham (Switzerland): Springer International; 2018.
[2] Genovese A, Garofano D, Sakhnevych A, et al. Static and dynamic analysis of non-Pneumatic tires based on experimental and numerical methods. Appl Sci. 2021;11(23):11232.
[3] Sakhnevych A. Multiphysical MF-based tyre modelling and parametrisation for vehicle setup and control strategies optimisation. Vehicle Syst Dyn. 2021;21:1–22. 10.1080/00423114.2021.1977833.
[4] O'Neill A, Prins J, Watts JF, et al. Enhancing brush tyre model accuracy through friction measurements. Vehicle Syst Dyn. 2021;115:1–23. 10.1080/00423114.2021.1893766.
[5] Romano L, Bruzelius F, Jacobson B. Unsteady-state brush theory. Vehicle Syst Dyn. 2020;59(11):1643–1671. 10.1080/00423114.2020.1774625.
[6] Romano L, Bruzelius F, Jacobson B. Brush tyre models for large camber angles and steering speeds. Vehicle Syst Dyn. 2020;21:1–52. 10.1080/00423114.2020.1854320.
[7] Romano L, Timpone F, Bruzelius F, et al. Analytical results in transient brush tyre models: theory for large camber angles and classic solutions with limited friction. Meccanica. 10.1007/s11012-021-01422-3.

[8] Pacejka HB. Tire and vehicle dynamics. 3rd ed. Amsterdam: Elsevier/BH; 2012.
[9] Bengt JHJ. Vehicle Dynamics Compendium. 2020. Available from: https://research.chalmers.se/en/publication/520229.
[10] von Schlippe B, Dietrich R. Das flattern eined bepneuten rades. Bericht 140 der Lilienthal Gesellschaft. 1941: NACA TM 1365.
[11] Segel L. Force and moment response of pneumatic tires to lateral motion inputs. Trans ASME J Eng Industry. 1966;88: 10.1076/vesd.41.1.1.23406.
[12] Pauwelussen JP. The local contact between tyre and road under steady state combined slip conditions. Vehicle Syst Dyn. 2004;41(1):1–26. 10.1076/vesd.41.1.1.23406.
[13] Takács D, Orosz G, Stépán G. Delay effects in shimmy dynamics of wheels with stretched string-like tyres. Eur J Mech- A/Solids. 2009;28(3):516–525.
[14] Takács D, Stépán G. Micro-shimmy of towed structures in experimentally uncharted unstable parameter domain. Vehicle Syst Dyn. 2012;50(11):1613–1630.
[15] Takács D, Stépán G, Hogan SJ. Isolated large amplitude periodic motions of towed rigid wheels. Nonlinear Dyn. 2008;52:27–34. 10.1007/s11071-007-9253-y.
[16] Takács D, Stépán G. Experiments on quasiperiodic wheel shimmy. ASME J Comput Nonlinear Dynam. 2009;4(3):031007. 10.1115/1.3124786.
[17] Takács D, Stépán G. Contact patch memory of tyres leading to lateral vibrations of four-wheeled vehicles. Phil Trans R Soc A. 2013; 37120120427. 10.1098/rsta.2012.0427.
[18] Besselink IJM. Shimmy of aircraft main landing gears [doctoral thesis]. Delft; 2000.
[19] Ran S. Tyre models for shimmy analysis: from linear to nonlinear [doctoral thesis]. Eindhoven; 2016.
[20] Pacejka HB. The wheel shimmy phenomenon: a theoretical and experimental investigation with particular reference to the non-linear problem [doctoral thesis]. Delft; 1966.
[21] Pacejka HB, Bakker E. The magic formula tire model. Int J Vehicle Mechanics and Mobility. 1992;21(1):1–18.
[22] Higuchi A. Transient response of tyres at large wheel slip and camber [doctoral thesis]. Delft; 1997.
[23] Higuchi A, Pacejka HB. The relaxation length concept at large wheel slip and camber. Vehicle Syst Dyn. 1997;25(sup001):50–64. 10.1080/00423119708969644.
[24] Maurice JP, Berzeri M, Pacejka HB. Pragmatic tyre model for short wavelength side slip variations. Vehicle Syst Dyn. 1999;31(2):65–94. 10.1076/vesd.31.2.65.2096.
[25] Rill G. Sophisticated but quite simple contact calculation for handling tire models. Multibody Syst Dyn. 2019;45:131–153. 10.1007/s11044-018-9629-4.
[26] Rill G. Road vehicle dynamics: fundamentals and modeling with MATLAB®. 2nd ed. Abingdon: CRC Press; 2020.
[27] Svendenius J, Wittenmark B. Brush tire model with increased flexibility. European Control Conference; Cambridge, UK: 2015. 10.23919/ECC.2003.7085237.
[28] Svendenius J. Tire modelling and friction estimation [dissertation]. Lund; 2007.
[29] Svendenius J, Gäfvert M, Bruzelius F, et al. Experimental validation of the brush tire model. Tire Sci Technol. 2009;37(2):122–137.
[30] Pacejka HB, Besselink IJM. Magic formula tyre model with transient properties. Vehicle Syst Dynam. 1997;27(Sup001):234–249. 10.1080/00423119708969658.
[31] Romano L, Sakhnevych A, Strano S, et al. A novel brush-model with flexible carcass for transient interactions. Meccanica. 2019;54:1663–1679. 10.1007/s11012-019-01040-0.
[32] Shaju A, Pandey AK. Modelling transient response using PAC 2002-based tyre model. Vehicle Syst Dyn. 2020; 10.1080/00423114.2020.1802048:
[33] Canudas-de-Wit C, Olsson H, Astrom KJ, et al. A new model for control of systems with friction. IEEE Trans Automat Contr. 1995;40(3):419–425. 10.1109/9.376053.
[34] Canudas-de-Wit C, Tsiotras P, Velenis E, et al. Dynamic friction models for road/tire longitudinal interaction. Vehicle Syst Dyn. 2003;39(3):189–226. 10.1076/vesd.39.3.189.14152.
[35] Canudas-de-Wit C, Tsiotras P. Dynamic tire friction models for vehicle traction control. Proceedings of the 38th IEEE Conference on Decision and Control (Cat. No. 99CH36304); Vol. 4, Phoenix, AZ, USA: 1999. p. 3746–3751. 10.1109/CDC.1999.827937.

[36] Velenis E, Tsiotras P, Canudas-de-Wit C, et al. Dynamic tyre friction models for combined longitudinal and lateral vehicle motion. Vehi Syst Dyn. 2005;43(1):3–29. 10.1080/00423110412331290464.
[37] Deur J. Modeling and analysis of longitudinal tire dynamics based on the Lugre friction model. IFAC Proceedings Volumes. 2001;34(1):91–96. 10.1016/S1474-6670(17)34383-5.
[38] Deur J, Asgari J, Hrovat D. A 3D brush-type dynamic tire friction model. Vehicle Syst Dyn. 2004;42(3):133–173. 10.1080/00423110412331282887.
[39] Deur J, Ivanovic V, Troulis M, et al. Extensions of the LuGre tyre friction model related to variable slip speed along the contact patch length. Vehicle Syst Dyn. 2005;43(supp):508–524. 10.1080/00423110500229808.
[40] Xu N, Guo K, Zhang X, et al. An analytical tire model with flexible carcass for combined slips. Math Probl Eng. 2014; 397538. Article ID 9 pages.10.1155/2014/397538.
[41] Liang W, Medanic J, Ruhl R. Analytical dynamic tire model. Vehicle Syst Dyn. 2008;46(3): 197–227. 10.1080/00423110701267466.
[42] Kikuuwe R. A brush-type tire model with nonsmooth representation. Math Probl Eng. 2019; 9747605. Article ID 13 Pages.10.1155/2019/9747605.
[43] Edwards CH. Advanced Calculus of Several Variables, III – Successive Approximations and Implicit Functions. Academic Press; 1973. P. 160–202.
[44] Bruzelius F, Hjort M, Svendenius J. Validation of a basic combined-slip tyre model for use in friction estimation applications. Proc Inst Mech Eng D J Automobile Eng. 2014;228(13):1622–1629. 10.1177/0954407013511797.
[45] Khalil HK. Nonlinear systems. 3rd. Upper Saddle River: Prentice Hall; 2002.

Appendices

Derivation of the sliding functions

The derivation of the sliding functions appearing in Equation (24) may be worked out similarly as in Romano et al. [5]. Substituting Equation (1) into Equation (18a), assuming vanishing sliding and disregarding the partial derivative with respect to the longitudinal coordinate yields, after some manipulations,

$$\begin{bmatrix} A_{\mathscr{P}}\mathbf{K}_{\boldsymbol{t}} & \mathbf{K}_{\boldsymbol{t}}\tilde{\mathbf{I}}\mathbf{S}_{\mathscr{P}} \\ \mathbf{I}_{\boldsymbol{\sigma}} & I_{\varphi} \end{bmatrix} \begin{bmatrix} \boldsymbol{\sigma} \\ \varphi \end{bmatrix} \approx \frac{1}{V_{\mathrm{r}}} \begin{bmatrix} \mathbf{I} + A_{\mathscr{P}}\mathbf{K}_{\boldsymbol{t}}\mathbf{S}' & \mathbf{0} \\ \mathbf{I}_{\boldsymbol{\sigma}}\mathbf{S}' & 1 \end{bmatrix} \begin{bmatrix} \dot{\boldsymbol{F}}_{\boldsymbol{t}} \\ \dot{M}_z \end{bmatrix}. \tag{A1}$$

where

$$A_{\mathscr{P}} \triangleq \iint_{\mathscr{P}} \mathrm{d}\boldsymbol{x}, \tag{A2a}$$

$$\mathbf{S}_{\mathscr{P}} \triangleq \iint_{\mathscr{P}} \boldsymbol{x}\,\mathrm{d}\boldsymbol{x} \tag{A2b}$$

$$\mathbf{I}_{\boldsymbol{\sigma}} = \begin{bmatrix} I_{\sigma_x} & I_{\sigma_y} \end{bmatrix} \triangleq \begin{bmatrix} \iint_{\mathscr{P}} k_{yx}x - k_{xx}y\,\mathrm{d}\boldsymbol{x} & \iint_{\mathscr{P}} k_{yy}x - k_{xy}y\,\mathrm{d}\boldsymbol{x} \end{bmatrix}, \tag{A2c}$$

$$I_{\varphi} \triangleq \iint_{\mathscr{P}} k_{yy}x^2 - (k_{xy} + k_{yx})xy + k_{xx}y^2\,\mathrm{d}\boldsymbol{x}, \tag{A2d}$$

and the matrix $\tilde{\mathbf{I}}$ reading

$$\tilde{\mathbf{I}} \triangleq \begin{bmatrix} 0 & -1 \\ 1 & 0 \end{bmatrix}. \tag{A3}$$

Solving Equation (A1) for the theoretical slip and spin variables yields

$$\begin{bmatrix} \boldsymbol{\sigma} \\ \varphi \end{bmatrix} \approx \frac{1}{V_{\mathrm{r}}} \begin{bmatrix} \check{\boldsymbol{\sigma}}\left(\dot{\boldsymbol{F}}_{\boldsymbol{t}}, \dot{M}_z\right) \\ \check{\varphi}\left(\dot{\boldsymbol{F}}_{\boldsymbol{t}}, \dot{M}_z\right) \end{bmatrix} \triangleq \frac{1}{V_{\mathrm{r}}} \begin{bmatrix} \mathbf{S}'_{\boldsymbol{F}} & \mathbf{S}'_{M} \\ \mathbf{S}'_{\varphi\boldsymbol{F}} & S'_{\varphi M} \end{bmatrix} \begin{bmatrix} \dot{\boldsymbol{F}}_{\boldsymbol{t}} \\ \dot{M}_z \end{bmatrix}, \tag{A4}$$

where the matrix of generalised compliances is defined as

$$\begin{bmatrix} \mathbf{S}'_{\boldsymbol{F}} & \mathbf{S}'_{M} \\ \mathbf{S}'_{\varphi \boldsymbol{F}} & S'_{\varphi M} \end{bmatrix} \triangleq \begin{bmatrix} A_{\mathscr{D}} \mathbf{K}_{\boldsymbol{t}} & \mathbf{K}_{\boldsymbol{t}} \tilde{\mathbf{I}} \mathbf{S}_{\mathscr{D}} \\ \mathbf{I}_{\boldsymbol{\sigma}} & I_{\varphi} \end{bmatrix}^{-1} \begin{bmatrix} \mathbf{I} + A_{\mathscr{D}} \mathbf{K}_{\boldsymbol{t}} \mathbf{S}' & \mathbf{0} \\ \mathbf{I}_{\boldsymbol{\sigma}} \mathbf{S}' & 1 \end{bmatrix}. \tag{A5}$$

Proof of Theorem 4.1

The proof of Theorem 4.1 is given here.

Proof: The result follows from an application of Theorem 4.19 ([45, Chapter 4]). For the problem under consideration, the Lyapunov function may be defined as $V(\boldsymbol{F}_{\boldsymbol{t}}(t)) \triangleq \frac{1}{2} F_{\boldsymbol{t}}^2(t)$. The above function satisfies the first assumption of Theorem 4.19 with $\alpha_1(F_{\boldsymbol{t}}) = \alpha_2(F_{\boldsymbol{t}}) = V(\boldsymbol{F}_{\boldsymbol{t}})$, which implies $\rho(\cdot) \equiv \gamma(\cdot)$. Taking the derivative yields

$$\dot{V}\left(\boldsymbol{F}_{\boldsymbol{t}}(t)\right) = -V_{\mathrm{r}}(t) \mathbf{C}'_{\boldsymbol{\sigma}} \hat{\boldsymbol{\sigma}}_{\epsilon}\left(\boldsymbol{F}_{\boldsymbol{t}}(t); \epsilon\right) \cdot \boldsymbol{F}_{\boldsymbol{t}}(t) + V_{\mathrm{r}}(t) \mathbf{C}'_{\boldsymbol{\sigma}} \boldsymbol{\sigma}(t) \cdot \boldsymbol{F}_{\boldsymbol{t}}(t). \tag{A6}$$

Since $V(\boldsymbol{F}_{\boldsymbol{t}}(t))$ is radially unbounded and $\dot{V}(\boldsymbol{F}_{\boldsymbol{t}}(t))$ is negative definite for $\boldsymbol{\sigma} = \mathbf{0}$, it may be easily concluded that the origin is asymptotically stable. Recalling that $\hat{\boldsymbol{\sigma}}_{\epsilon}(\boldsymbol{F}_{\boldsymbol{t}}; \epsilon) = \hat{\sigma}(F_{\boldsymbol{t}}) \boldsymbol{F}_{\boldsymbol{t}} / (F_{\boldsymbol{t}} + \epsilon)$, Equation (A6) yields

$$\begin{aligned}
\dot{V}\left(\boldsymbol{F}_{\boldsymbol{t}}(t)\right) &= -V_{\mathrm{r}}(t) \hat{\sigma}\left(F_{\boldsymbol{t}}(t)\right) \frac{\mathbf{C}'_{\boldsymbol{\sigma}} \boldsymbol{F}_{\boldsymbol{t}}(t) \cdot \boldsymbol{F}_{\boldsymbol{t}}(t)}{F_{\boldsymbol{t}}(t) + \epsilon} + V_{\mathrm{r}}(t) \mathbf{C}'_{\boldsymbol{\sigma}} \boldsymbol{\sigma}(t) \cdot \boldsymbol{F}_{\boldsymbol{t}}(t) \\
&\leq -V_{\mathrm{r}}(t) \hat{\sigma}\left(F_{\boldsymbol{t}}(t)\right) \frac{\mathbf{C}'_{\boldsymbol{\sigma}} \boldsymbol{F}_{\boldsymbol{t}}(t) \cdot \boldsymbol{F}_{\boldsymbol{t}}(t)}{F_{\boldsymbol{t}}(t) + \epsilon} + V_{\mathrm{r}}(t) \left\| \boldsymbol{\nu}'_{\boldsymbol{\sigma}} \boldsymbol{\sigma}(t) \cdot \boldsymbol{F}_{\boldsymbol{t}}(t) \right\|_2 \\
&\leq -V_{\mathrm{r}}(t) \lambda_{\min}\left(\mathbf{C}'_{\boldsymbol{\sigma}}\right) \hat{\sigma}_{\epsilon}\left(F_{\boldsymbol{t}}(t); \epsilon\right) F_{\boldsymbol{t}}(t) + V_{\mathrm{r}}(t) \sigma(t) \left\| \boldsymbol{\nu}'_{\boldsymbol{\sigma}} \boldsymbol{F}_{\boldsymbol{t}}(t) \right\|_2 \\
&\leq -V_{\mathrm{r}}(t) \lambda_{\min}\left(\mathbf{C}'_{\boldsymbol{\sigma}}\right) \hat{\sigma}_{\epsilon}\left(F_{\boldsymbol{t}}(t); \epsilon\right) F_{\boldsymbol{t}}(t) + V_{\mathrm{r}}(t) \lambda_{\max}\left(\mathbf{C}'_{\boldsymbol{\sigma}}\right) \sigma(t) F_{\boldsymbol{t}}(t) \\
&= -W\left(F_{\boldsymbol{t}}(t), t\right) - V_{\mathrm{r}}(t) \psi \lambda_{\min}\left(\mathbf{C}'_{\boldsymbol{\sigma}}\right) \hat{\sigma}_{\epsilon}\left(F_{\boldsymbol{t}}(t); \epsilon\right) F_{\boldsymbol{t}}(t) + V_{\mathrm{r}}(t) \lambda_{\max}\left(\mathbf{C}'_{\boldsymbol{\sigma}}\right) \sigma(t) F_{\boldsymbol{t}}(t),
\end{aligned} \tag{A7}$$

where $W(F_{\boldsymbol{t}}(t), t) \triangleq V_{\mathrm{r}}(t)(1 - \psi) \lambda_{\min}(\mathbf{C}'_{\boldsymbol{\sigma}}) \hat{\sigma}_{\epsilon}(F_{\boldsymbol{t}}(t); \epsilon) F_{\boldsymbol{t}}(t)$ is positive definite for some positive constant $\psi \in (0, 1)$. Therefore, any value of $F_{\boldsymbol{t}}(t)$ such that

$$\hat{\sigma}_{\epsilon}\left(F_{\boldsymbol{t}}(t); \epsilon\right) \geq \frac{\sigma(t)}{\psi \chi_{\lambda}} \tag{A8}$$

ensures that $\dot{V}(\boldsymbol{F}_{\boldsymbol{t}}(t))$ is negative definite. Reversing the inequality, it may be deduced that if

$$\sup_{t \geq t_0} \sigma(t) < \theta \chi_{\lambda} \hat{\sigma}_{\epsilon}\left(\mu_{\text{peak}} F_z; \epsilon\right) = \psi \chi_{\lambda} \sigma^{\text{peak}} \frac{1}{1 + \epsilon\left(\mu_{\text{peak}} F_z\right)} \triangleq \sigma_{\chi}, \tag{A9}$$

then $F_{\boldsymbol{t}}(t) < \mu_{\text{peak}} F_z$ for all $t \geq t_0$.

Furthermore, since $\hat{\sigma}_{\epsilon} : [0, \mu_{\text{peak}} F_z) \mapsto [0, \sigma_{\chi} / (\psi \chi_{\lambda}))$ is a $\mathcal{K}$-class function in $(0, \mu_{\text{peak}} F_z)$ by Assumption 3.2, its inverse $\sigma_{\epsilon}^{-1}(\cdot; \epsilon)$ may be computed in $(0, \mu_{\text{peak}} F_z)$. The function

$$\gamma(\sigma; \epsilon) \triangleq \begin{cases} 0, & \sigma = 0, \\ \sigma_{\epsilon}^{-1}\left(\dfrac{\sigma}{\psi \chi_{\lambda}}; \epsilon\right), & \sigma \in \left(0, \sigma_{\chi}\right), \end{cases} \tag{A10}$$

is continuous in $[0, \sigma_{\chi})$, since $\hat{\sigma}_{\epsilon}(0; \epsilon) = 0$ and $\lim_{F_{\boldsymbol{t}} \to \mu_{\text{peak}} F_z} \hat{\sigma}_{\epsilon}(F_{\boldsymbol{t}}; \epsilon) = \sigma_{\chi} / (\psi \chi_{\lambda})$. Additionally, it is strictly increasing. Therefore, it may be concluded that $\gamma \in \mathcal{K}$. Then, it may be observed that, when $\sigma = 0$, $F_{\boldsymbol{t}} = 0$ satisfies automatically the inequality, since it is $\sigma_{\epsilon}(0; \epsilon) = 0 \equiv \gamma(0; \epsilon)$. On the

other hand, for $\sigma \in (0, \sigma_\chi)$ it holds that

$$F_{\boldsymbol{t}} = \hat{\sigma}_\epsilon^{-1} \circ \hat{\sigma}_\epsilon(F_{\boldsymbol{t}}; \epsilon) \geq \hat{\sigma}_\epsilon^{-1}\left(\frac{\sigma}{\psi\chi_\lambda}; \epsilon\right) \triangleq \gamma(\sigma; \epsilon). \tag{A11}$$

Therefore, it may be inferred that the system (41) is input-to-state-stable with $\gamma(\cdot; \epsilon)$ defined as in Equation (A10). It remains to prove that $\gamma(\sigma; \epsilon) \to F_{\boldsymbol{t}}^{-1}(\sigma/(\psi\chi_\lambda))$ as $\epsilon \to 0^+$. The result for $\sigma = 0$ is trivial. In any other case:

$$\lim_{\epsilon \to 0^+} \gamma(\sigma; \epsilon) = \lim_{\epsilon \to 0^+} \hat{\sigma}_\epsilon^{-1}\left(\frac{\sigma}{\theta\chi_\lambda}; \epsilon\right) = \hat{\sigma}^{-1}\left(\frac{\sigma}{\psi\chi_\lambda}\right) = \hat{F}_{\boldsymbol{t}}\left(\frac{\sigma}{\psi\chi_\lambda}\right). \tag{A12}$$

■